Numerical analysis of a three-leaflet aortic valve prosthesis

de Hart, J.

Award date:
1997

Numerical Analysis of a Three-Leaflet Aortic Valve Prosthesis

Jürgen de Hart

WFW report 97.026
Master's Thesis

Coaches:
drs. G. Cacciola
dr. ir. P. Schreurs
dr. ir. G. Peters

prof. dr. ir. J.D. Janssen
prof. dr. ir. F.P.T. Baaijens

Department of Mechanical Engineering
Eindhoven University of Technology

April 1997

Numerical Analysis of a Three-Leaflet Aortic Valve Prosthesis

Jürgen de Hart

April 14, 1997

Master's Thesis

WFW-Report 97.026

Coaches:
Drs. G. Cacciola
Dr. Ir. P. Schreurs
Dr. Ir. G. Peters

Department of Mechanical Engineering
Eindhoven University of Technology, The Netherlands

Contents

Abstract

A new aortic valve prosthesis is under development, which should combine a high degree of mobility with high strength and stiffness in a closed configuration. The prosthesis is designed for better durability of mechanical and hemodynamic performance. It has three leaflets of rubber reinforced with polyethylene (PE) fibers, which are attached to a rigid nylon stent. The leaflets-stent combination shows a cylindrical open stress-free configuration. Like for the natural valve, it is suggested that appropriate fiber reinforcements reduce stresses in the weaker parts of the leaflets. It is expected that these reduced stresses result in a decrease of tears and perforation of the leaflets. To prevent expensive and time consuming experiments numerical simulations are desired to predict the behaviour of reinforced testing models under simulated physiological load.

A numerical model of the three-leaflet reinforced synthetic valve prosthesis has been developed using MARC FEM techniques. The dimensions of the prosthesis are used as input data for this model. Different fiber reinforcements are implemented using Matlab 4.2 and MENTAT II 3.1. The leaflets are modeled as a composite structure of fiber and rubber material. Since no fluid interactions are taken into account, deformation is realized by applying a static uniform pressure on the leaflet, as measured experimentally from the pressure difference between aorta and ventricular side of the valve. 'Path-Following' solution algorithms are used to solve the model, which shows instabilities caused by its 'snap-through' behaviour.

Numerical simulations are performed of simple experimental tensile and bending tests on leaflet material structures, in order to gain confidence about the leaflet material modeling. From the results it is concluded that the implementation of fiber reinforced materials satisfies the experimental outcome of corresponding structures.

Numerical solution problems occurred for the model of the three-leaflet valve prosthesis in some cases of fiber reinforcement. Two adjustments are introduced in the model that led to convergent simulations for all fiber reinforcements discussed in the report. The longitudinal fiber modulus is taken 10% of the original value and the applied pressure load is taken 33% of the maximum difference measured experimentally.

The effect of a lower longitudinal fiber modulus is investigated numerically. It is observed that stress distributions are not affected by a decrease of this fiber modulus. However, stress values should be interpreted carefully for the prediction of stress values in leaflets of the aortic valve prosthesis.

Results of a closed non-reinforced model are compared to results of [Black, 1991], [Chandran, 1991] and [Krucinski, 1993]. It is observed that all models show similar areas of high stresses. However, stress values are very different, since different material properties are used for the leaflets and, since a different pressure load is applied to the leaflets. The deformation of a fiber reinforced model is compared to the deformation of a corresponding prosthesis and as a result, very similar deformations are obtained.

Responses of fiber reinforced models are analyzed for stresses that are expected to contribute to the failure of the valve prosthesis. It is concluded that fiber reinforcements reduce stresses in the weaker parts of the leaflet structure and show, in some cases, a more homogeneous stress distribution compared to non-reinforced models. However, from the results it is concluded that no fiber reinforcement discussed in this report is categorized as the most appropriate for use in valve prostheses.

Chapter 1

Introduction

The human aortic heart valve is a passive device that opens and closes in response to changes in pressure to maintain the unidirectional flow of blood from the ventriculus to the aorta. When functioning normally, it is extremely efficient, having minimal resistance to forward flow and allowing only trivial backflow when closed. In certain situations, the efficiency of the valve may be severely affected. Pathological changes through valve disease may result in a restriction of the free opening of the valve (stenosis) or a loss of competence allowing backflow through the closed valve (regurgitation). Replacement with artificial heart valves may then improve cardiovascular performance, long-term survival and quality of life. Currently, there are three different types of heart valve prostheses with their own advantages and disadvantages:

1. The mechanical prostheses, in which a ball, disc or rigid leaflets regulate the blood flow. These prostheses have a long-term durability. However, the natural blood flow is affected by the valvular geometry and material used which results in high incidence of thromboembolism and therefore, long-term anticoagulant therapy is inevitable [19]. Moreover, mechanical prostheses have a considerable pressure gradient over the valve, which causes the heart to contract stronger in order to maintain the normal pressure gradient.

2. The biological prostheses, which have three flexible leaflets of biological origin, suspended in a flexible or non-flexible frame. These prostheses allow a more natural blood flow and thus a low incidence of thromboembolism. Furthermore, the pressure gradient over the valve is much lower which reduces valve damaging [19], [21]. However, tissue failure caused by calcification results in a short lifetime.

3. The artificial synthetic prostheses, which consist of two or three flexible leaflets made of synthetic material. Advantages and disadvantages of these prostheses are comparable to those of the biological valve prostheses, however, an additional advantage is that the synthetic leaflets can be redesigned to reduce stresses which appear during functioning. These prostheses are only used in short-term applications, such as artificial blood pumps, heart assist devices and artificial hearts. At this moment the valves are not reliable for long-term applications [19].

In view of the disadvantages of the different prostheses, it is not possible to categorize any particular valve as the best. A good valve prosthesis should have the durability of a mechanical and the hemodynamic performance of a biological valve without the need for

anticoagulant therapy. Excellent hemodynamic performance is accomplished using flexible leaflets. However, the mechanical performance is compromised because of significant mechanical stresses in the closed and open situation of the valve resulting in tears and perforations in the leaflets. One of the natural stress reducing mechanisms is fiber reinforcement of the leaflets with collagen and elastin fibers. The fiber reinforced structure of the aortic valve leaflet combines a high degree of mobility during opening and closing with a great strength and stiffness in the closed situation.

Within the Department of Mechanical Engineering of the Eindhoven University of Technology a new design for a synthetic valve is under development which should meet with these characteristics of the aortic valve. This is a three-leaflet valve with rubber used as matrix material reinforced with polyethylene (PE) fibers. In order to reduce unfavourable mechanical stresses that occur in the leaflets during deformation, the fiber layout over the leaflets will be adapted. To prevent expensive and time consuming experiments numerical simulations are desired to predict the behaviour of testing models under simulated physiological load.

The purpose of this study is to develop a numerical model of the artificial fiber reinforced aortic valve using FEM techniques. The influence of different fiber reinforcements on the stress distribution over the leaflets is analyzed. Considering failure mechanisms for the leaflet material structure, fiber layouts can be defined for the real aortic valve prosthesis, resulting in a prototype with better durability of mechanical performance.

When designing a prosthetic heart valve it is necessary to have knowledge about the structure and function of the natural valve. A summary of relevant basic information on the anatomy and physiology of the aortic heart valve is given in the next chapter. In chapter 3 is described the development, production and testing of the aortic heart valve prosthesis in the laboratory of the Eindhoven University of Technology. The modeling of the prosthesis, using numerical techniques, is described in chapter 4. Within this computer model the geometric and material properties of the valve prosthesis are taken into account as well as the mechanical boundary conditions. The physiological load of the valve prosthesis during testing is implemented as a mechanical load over the leaflets. In chapter 5 numerical results are presented of models with different fiber reinforcements over the leaflets. Finally, conclusions and recommendations about the numerical procedure and results are presented in chapter 6.

Chapter 2

Anatomy and Physiology of the Aortic Heart Valve

2.1 Introduction

Knowledge about the anatomy and functioning of the aortic valve is required when designing a prosthetic heart valve. In this chapter a survey is given on these features based on the literature. Anatomical and histological aspects are discussed in the next sections as well as prominent mechanical and kinematical properties in relation to valve functioning. With this information more understanding is obtained about the function of the different components of the aortic valve during the cardiac cycle.

2.2 The Anatomy of the Aortic Valve

The human heart is a pump with four chambers, located in the middle of the chest, with the apex inclined slightly towards the left side. At the right side of the heart deoxygenated blood returns from the superior and inferior branches of the vena cava (Fig. 2.1), and drains into the right atrium which is normally at a low pressure. At the left side oxygenated blood from the lungs arrives at the left atrium from the pulmonary vein. During diastole, the relaxation phase of the cardiac cycle, blood flows through the tricuspid valve into the right ventricle and through the mitral valve into the left ventricle pushing the leaflets aside. At systole, the pumping phase of the heart, both ventricles start to contract and the intraventricular pressure increases. This causes the leaflets of the tricuspid valve and the mitral valve to snap shut and the cusps of the pulmonary valve and aortic valve to open. Blood then flows out of the ventricles through the pulmonary artery to the lungs and through the aorta to feed the systematic circulation. As the ventricles relax, the pressure in the right ventricle drops below the pressure in the pulmonary artery and the pressure in the left ventricle drops below the pressure in the aorta, causing the pulmonary valve and the aortic valve to close and the ventricles to begin filling again.

While the basic geometry and function of the two sides of the heart are very similar, they have different tasks. The right side supplies blood only to the lungs, while the left must pump blood to the rest of the body. It is not surprising that the left side of the heart must develop much higher pressures than the right side. This most certainly contributes to the fact that heart valves on the left side of the heart are most often affected by disease, especially the

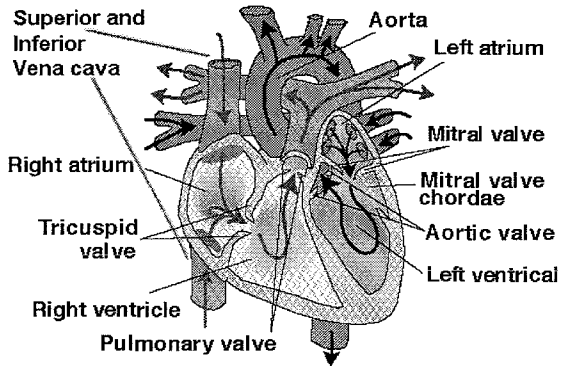

Figure 2.1: *The basic anatomy of the heart.*

aortic valve.

The aortic valve, situated at the outlet of the left ventricle, is one of the four cardiac valves controlling blood flow through the heart. The valve consists of three anatomical entities: three leaflets, three sinus cavities and the aortic ring (Fig. 2.2) [21]. The leaflets are thin flaps of flexible, tough endothelium-covered fibrous tissue firmly attached at the base to the fibrous valve rings. Two functional areas can be distinguished in each leaflet. One area, near the free edge, is known as the lunula, thanks to its semilunar shape. When the valve is closed, the outlet orifice of the left ventricle is sealed because the lunulae of adjacent leaflets are coincident with each other. The remainder area of the leaflet surface, not making contact with adjacent leaflets when the valve is closed, is referred to as the load bearing leaflet portion [13]. Halfway the free leaflet edge there is a thickening, the so-called corpus Aranti (Fig. 2.3). The line of attachment of the leaflets to the aortic wall will be referred to as the aortic ring or annulus fibroses. This attachment forms a U-shaped arch of which the tops, where the lunulae of adjacent leaflets merge into the aortic ring, are called commissures. Behind each leaflet the aortic wall expands to form three dilated pouches, the sinuses of Valsalva, the wall of which are considerably thinner than the aorta wall. In two of the three sinuses the orifices of the coronary arteries are located, which supply the heart muscle with blood. The two anterior sinuses (and leaflets) are commonly denoted as the right and left coronary sinus (and leaflet). The third is the non-coronary or posterior sinus (and leaflet). Histological aspects of the different components are discussed in the next section [8].

2.3 Histological Aspects of the Aortic Valve

In the leaflets many macroscopically visible connective tissue bundles are present (Fig. 2.4) [21]. Originating at the commissures they run circumferentially like the free leaflet margin. Towards the leaflet center they show many ramifications, centrally forming a dense interwoven network of fine fibers. This directionality results in a structure that is considerably stiffer in the circumferential than the radial direction. In addition to these commissural fibers, discrete macroscopically visible bundles, perpendicular to the attachment line, anchor the middle portion of the leaflet to the aortic wall. In the aortic wall these bundles diverge into a fibrocartilaginous tissue which forms a U-shaped arch in each sinus as part of the aortic ring with increasing diameter from commissures towards the bottom of the sinus.

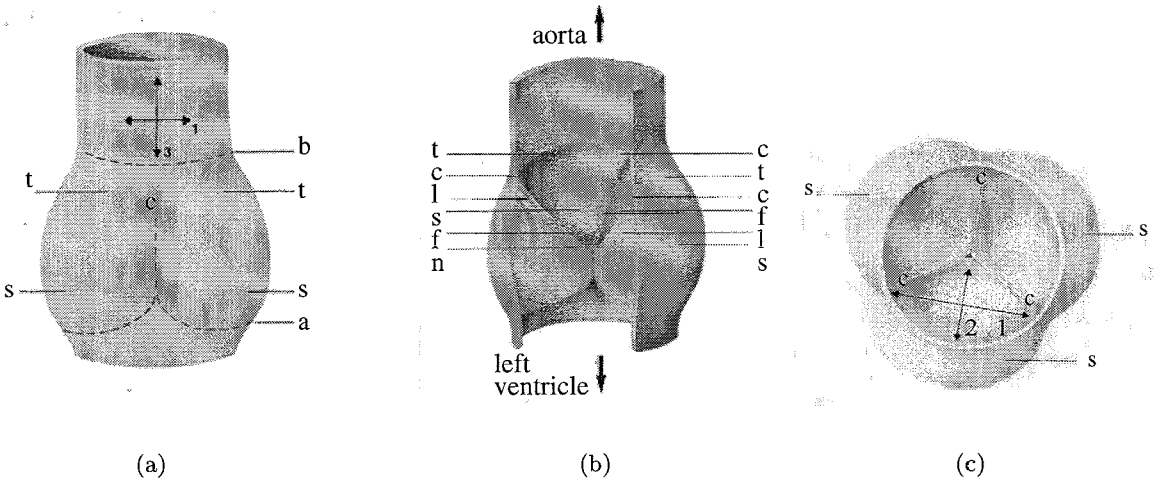

Figure 2.2: *(a) Side view of the valve. The dashed line a represents the aortic ring. (b) Side view after dissection of one leaflet and the corresponding sinus wall. (c) The aortic valve in closed configuration as seen from the aortic side (the coronary arteries are not shown) [21].*
c: commissure; f: free edge of leaflet; l: lunula; n: node of Arantius; s: sinus wall; t: top of sinus cavity; 1: circumferential direction; 2: radial direction; 3: axial direction

Within the endothelium of the leaflet, three different layers are immediately discernible (Fig. 2.5). The subendothelial ventricular layer (ventricularis) at the ventricular leaflet side is composed of elastin and collagen fibers, oriented in various directions. This layer is continuous with the subendothelian elastic tissue of the ventricle. The second layer consists of loose connective tissue structure, containing glycosaminoglycans (GAG's) and a few elastin fibers. This structure is continuous with the loose connective tissue in the attachment line in the aortic wall. The third layer contains the already mentioned coarse bundles of tightly packed collagen fibers. Some elastin fibers are present between these bundles, increasing in number towards the aortic side [20].

The lunulae of the leaflets are much thinner than the load bearing parts and although the same tissue components are present, their arrangement is very irregular at most sites and

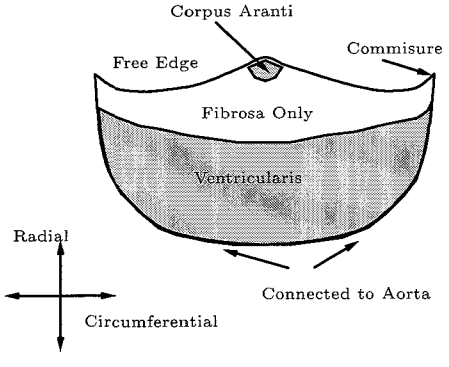

Figure 2.3: *Schematic presentation of the cusp anatomy.*

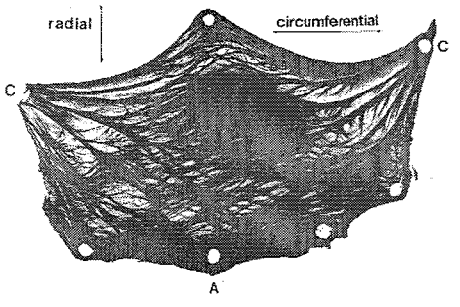

Figure 2.4: *Typical collagen bundle structure of the aortic leaflet. The leaflet is dissected from the aortic wall along the line C-A-C [21].*

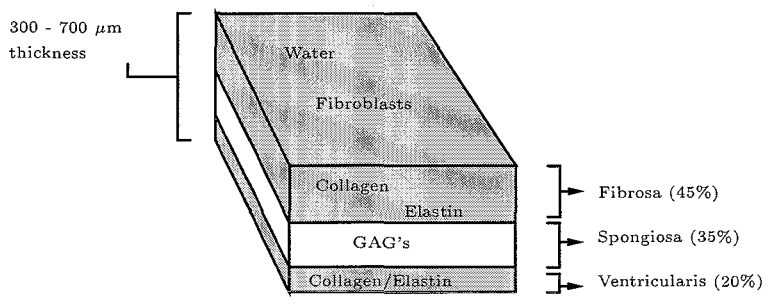

Figure 2.5: *Schematic cross section of the aortic cusp.*

varies from valve to valve. In some areas only loose connective tissue with a small number of elastin fibers can be seen, while in other areas the cross section of the leaflet consists exclusively of tightly packed collagen fibers of the macroscopically visible commissural bundles.

The sinus walls consist of mainly circumferentially arranged muscular tissue embedded in a network of arbitrarily oriented elastin fibers. Collagenous components are almost absent in the sinus walls and as far as the elastic parts are concerned, the sinus tissue will be rather compliant. In addition to their importance in the hydrodynamical functioning of the aortic valve, the sinus walls have also a mechanical function (section 2.4) [20].

2.4 Mechanical and Kinematical Aspects of the Aortic Valve

The shape of the aortic leaflet is of particular interest when its relationship to function is considered. During a human lifetime the aortic valve may open and close 3×10^9 times [13]. The fact that medical science has been unable to duplicate this function suggests that still there is not enough knowledge about the stress to which the normal valve is subjected.

Both mechanical and kinematical aspects are involved in valve functioning and differ in importance in the various phases of the cardiac cycle. During one cardiac cycle three main phases can be distinguished in valve performance: the opening and closing phases in systole and the diastolic phase during which the valve is closed. In the normal situation valve opening is very fast. The leaflets bulge towards the aorta just before left ventricular ejection begins. The valve is completely open when the peak flow in the ascending aorta has reached 75% of its maximum. As to valve closing two phases can be distinguished. The first is gradual closing of the valve that starts during the deceleration of aortic flow, resulting in about 80% valve closure at the moment of zero flow in the ascending aorta at end-systole. Finally, a small reversed flow completes closure [19]. A representative outline of the course of the aortic and left ventricular pressure, causing the blood flow, is given in Fig. 2.6.

Being thin and membrane-like structures (section 2.3), the valve leaflets cannot withstand any significant pressure difference during the opening and first closing phase. During these phases the leaflets may be expected to move in an essentially kinematical process governed by the fluid motion. Stresses resulting from pressure-loading, boundary-layer and inertia effects will be insignificant in these phases compared with the stresses to be expected in the second closing phase and during diastole [13]. In the course of diastole the leaflets have to withstand a slowly varying but none the less considerable pressure load.

In the functioning human aortic valve, the leaflets usually have been considered to be under stress in the closed position and stress-free in the open position, responding passively

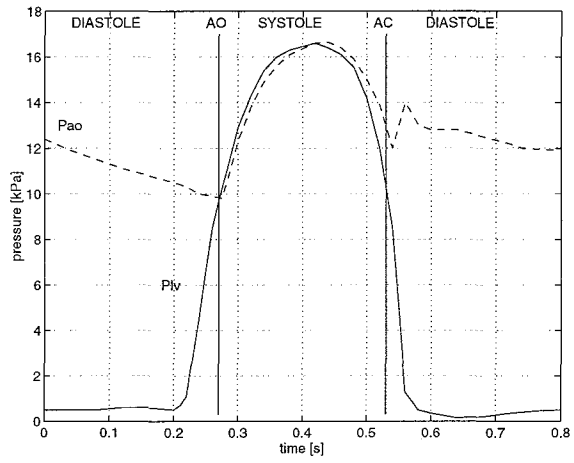

Figure 2.6: *Representative outline of the aortic (P_{ao}) and left ventricular (P_{lv}) pressures during the cardiac cycle.*
AO: aortic valve opens; AC: aortic valve closes.

to changes in the pressure gradients generated by the left ventricle. Direct observation of the functioning valve, however, indicates that the open valve assumes a triangular orifice. This configuration implies that the open leaflet is under significant stress [13]. The concept of normal aortic valve function is that the aortic root expands as the aortic valve opens and brings the leaflet orifice to triangular configuration. As the pressure falls the aortic root radius decreases and the leaflets flex towards the axis of the aorta, resulting in a valve closure. The relative incompliant leaflet is protected from fatigue of repeated lengthening and shortening by the changing dimensions of the aortic root [3]. The leaflet suspended from the aortic root, undergoes a relatively constant stress maintained during the cardiac cycle by motion of its supporting structure. This results in a considerable reduction in the fluctuation of the stresses placed on the leaflet and could explain how the leaflets last a lifetime under normal operating conditions.

The presence of the sinuses of Valsalva does affect aortic valve function, because of the effects on fluid flow, as well as stress distribution on the leaflets. Studies demonstrated that the sinus walls move outwards during diastole, implying that part of the load on the leaflets is taken up by the sinus walls [13]. This stress sharing decreases the stress and the wear on the leaflets. In each cardiac cycle, when ventricular pressure equals aortic pressure, the aortic root dilates and the intercommissural distances increase. When the root is not dilated, the functioning and geometry of the leaflets become abnormal and high open leaflet deformations occur. This causes high leaflet bending deformations that can lead to calcification [3].

During ventricular systole the cusps do not lie back against the wall of the aorta but float in the bloodstream approximately midway between the vessel walls and their closed position. In the sinuses of Valsalva, vortices develop that tend to keep the leaflet away from the vessel walls so the coronary ostia behind the coronary cusps can not be blocked. Vortices have a complex role in controlling the aortic valve during systole. The vortices provide a control mechanism for the valve to aid closure in the latter part of the systole. At peak systole, the blood flow into the sinuses from the aorta is matched by the blood flow out, and the aortic pressure-gradient vanishes. At this point, the leaflets are balanced between the sinus vortices and aortic flow. When the aortic flow decelerates, pressure in the aorta at the level of the

distal end of the sinuses exceeds that at the proximal end. Since blood enters the sinuses from the distal end, the average pressure in the sinuses exceeds that in the aorta, and the leaflets respond to this pressure-difference by moving towards closure, with blood flowing into the sinuses, but no longer out. At the end of the reduced ejection phase of ventricular systole, there is a brief reversal of blood flow towards the ventricles that snaps the cusps together and prevents regurgitation of blood into the ventricles.

Chapter 3

Development of a Synthetic Fiber Reinforced Three-Leaflet Heart Valve

3.1 Introduction

A design of an improved aortic valve prosthesis is recently developed, based upon a fundamental understanding of the behaviour of the natural valve (chapter 2). This prosthesis is a three-leaflet valve, which enables the use of the three natural sinuses. This chapter is focussed on the design and manufacturing of a prototype valve prosthesis. The geometry of the prosthesis and the materials used are discussed and experimental methods for the testing of the prosthesis are described. First, a brief review of currently developed heart valve prostheses and their failure phenomena is given in the next section.

3.2 Leaflet Valve Prostheses and Their Failure Behaviour

Disfunctioning heart valves are frequently replaced by heart valve prostheses. Commercially available prostheses are, up to now, either mechanical or biological. The mechanical ones are mostly disc-type prostheses and the biological prostheses usually have two or three flexible leaflets suspended in a flexible or non-flexible frame (chapter 1). These valves can be constructed from porcine valves or from bovine pericardium.

Currently, a new generation of heart valve prostheses is under development: the synthetic valves. The leaflets are mostly made of polyurethane. They are attached to a stent which can be more or less flexible. The intention is to endeavour the combination of all advantages of both mechanical and biological valves (chapter 1), excluding their disadvantages, but, up to now, there are still some problems. From experiments, it has been observed that also these valves show tears and calcification, and related fatigue failure, especially in the areas with the higher cycle stresses [1], [26].

In general three failure phenomena in biological and synthetic valve prostheses are observed (Fig. 3.1): (1) tears and perforations into the central portion of the leaflets, (2) tears in the leaflets in the vicinity of the commissures and (3) calcification in the central leaflet regions and at the base along the leaflet attachment. It is hypothesized that the tears and perforations in the central part of the leaflet in the vicinity of the leaflet attachment are caused

by high bending strains. The second failure phenomena could be caused by the high tensile stresses during the closed phase of the cardiac cycle. Finally, the regions of calcification in the leaflets correspond to the regions of high bending strains [19].

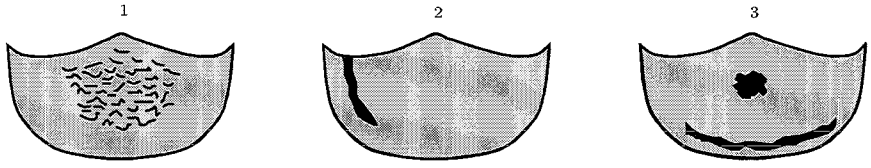

Figure 3.1: *The failure phenomena of leaflet heart valve prostheses [19].*

The natural aortic valve shows a few stress reducing mechanisms to prevent failure (section 2.4):

- Gradual valve closure.
- Leaflet reinforcement. The fiber reinforced structure of the aortic valve leaflet combine a high degree of mobility during opening and closing with high strength and stiffness in the closed situation.
- Thin fibers form the load carrying structure. The leaflets can be kept thin and thus bending stresses will be low.
- Flexible leaflet suspension. The aortic ring, to which the leaflets are suspended, changes shape during the cardiac cycle.

The three-leaflet synthetic valve prosthesis currently being developed at the Eindhoven University of Technology tries to take these stress reducing mechanisms into account. The prosthesis consists, at this point, of three flexible leaflets mounted on a relatively rigid stent. In the next section the materials used for the prosthesis are discussed. The valve design and manufacturing is described in section 3.4.

3.3 Materials

3.3.1 The Leaflets

The leaflets of the valve prosthesis are made of composite material consisting of a matrix of ethylene-propylene-diene-monomer (EPDM) rubber reinforced with polyethylene (PE) fibers (Fig. 3.2). The EPDM rubber plays the role of the connective tissue in the natural valve (section 2.3) and the PE fibers play the role of the collagen bundles if they are oriented in circumferential direction, or the role of elastin fibers if they follow a more random pattern.

EPDM rubber is a copolymer of ethylene and propylene. The third monomer (a diene) provides the ethylene-propylene rubbers with unsaturated side groups, so EPDM can be vulcanized and therefore, exhibits a high flex life [17]. Furthermore, the rubber has good heat and oxygen resistance, due to the low level of unsaturation. EPDM has been shown to be durable, especially in flexure, and can be processed in virtually any shape. Moreover, this material can be combined with polyethylene fibers. For the use in heart valve prostheses it is very suitable as matrix material of the flexible leaflets. Besides the favourable mechanical

properties and the high chemical stability, EPDM shows a good blood compatibility and a low swell-grade in blood. EPDM K320 is used with a composition of ethylene (55%), propylene (40.5%) and dicyclopentadiene (DCPD) (4.5%), containing dibenzoyl-peroxide as a crosslinker. It is assumed to have an incompressible isotropic linear elastic material behaviour, for the magnitudes of strains expected to occur, with a Young's modulus of $E_m = 1.5$ MPa, an associated shear modulus $G_m = 0.5$ MPa and a Poisson's ratio of $\nu_m = 0.5$ [17].

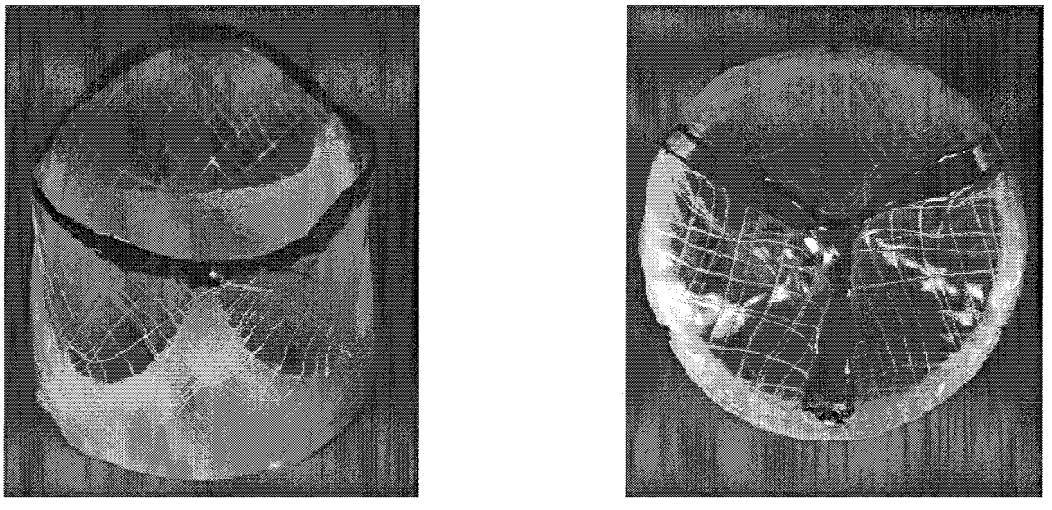

(a) (b)

Figure 3.2: *Prototype of a three-leaflet valve prosthesis with sinusoidal fiber reinforcement; (a) open position and (b) nearly closed position from top view.*

PE $(CH_2{-}CH_2)_n$ is a biocompatible crystalline polymer, because of its chain regularity, obtained after polymerization of the gas ethylene $(CH_2 {=} CH_2)$ [23]. With a solution (gel)-spinning process high-performance polyethylene (HP-PE) fibers can be made [18]. In these HP-PE fibers the weak Van der Waals interactions, operative between the chains in the oriented fiber, result in a highly anisotropic, one-dimensional structure. The HP-PE fibers have a high longitudinal Young's modulus, high elongation-to-break and low density. These characteristics make them suitable for applications in valve prostheses, as a representation of the fiber reinforced structure of the natural leaflets. In the three-leaflet valve prosthesis HP-PE fiber is used, which is assumed to have an orthotropic linear elastic material behaviour with an experimentally determined Young's modulus in longitudinal direction of $E_L = 30$ GPa (further referred to as E_f) and a diameter of 0.06 mm. The longitudinal shear modulus is $G_L = 640$ MPa (G_f) and the longitudinal-transversal Poisson's ratio is $\nu_{LT} = 0.4$ (ν_f) [23].

3.3.2 The Stent

The stent can be made of relatively stiff material or a very compliant material like rubber. The prosthesis discussed in this chapter consists of a rather rigid stent made of nylon 6 (polyamide (6), the 6 corresponds with the number of C-atoms in the monomers) by cutting it from a tube. Nylon 6 is very readily modified by use of monomer mixtures leading to copolymers. Key characteristics of nylon are its outstanding resistance to solvents, fatigue,

repeated impact and abrasion. Nylon 6 is isotropic with a tensile strength of 63 MPa. It is biological inert and has a high stiffness with respect to the leaflet material. Therefore, the stent is considered to be relatively rigid. More information about nylon 6 is found in [7].

3.4 Design and Manufacturing

A cylindrical steel mold is used to manufacture an open valve. The nylon stent is mounted on the mold, in a stent-shape incision, in such a way that the composition of mold and stent forms a cylinder. The mold with stent is dipped in a rubber solution several times while it is kept rotating by a motor (Fig. 3.3); the number of times it is dipped depends on the desired thickness. During drying, the rubber layer adheres to the stent. In order to prevent the rubber from sticking on the steel, a polymeric coating (Frekote, Dexter) is put on the mold before starting the procedure. After drying, a winding procedure is performed to put the fibers over the stent. The fibers are pre-wetted in a bath filled with the rubber solution and then wound from the fiber bobbin through a position controlling eye onto the mold. With a steel polymer coated pressing cylinder, the fiber is pressed on the rubber layer in the contact point (Fig. 3.3).

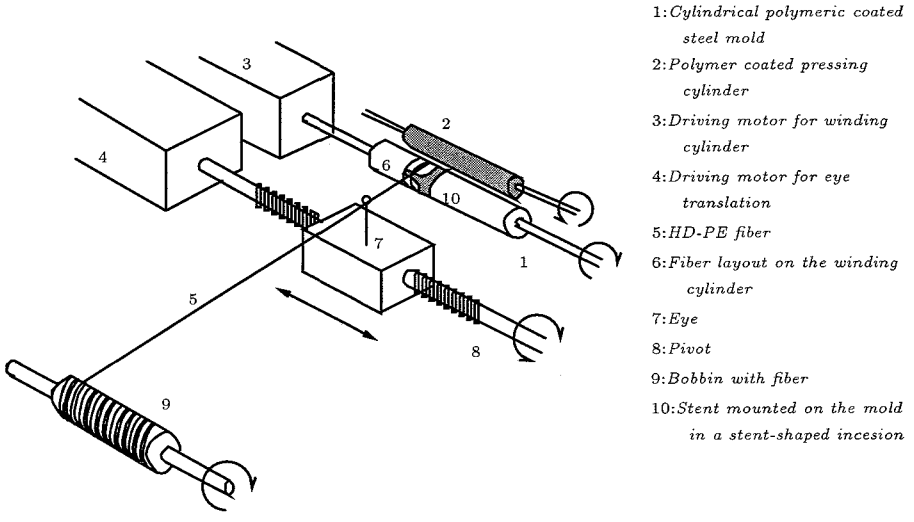

Figure 3.3: *Schematic presentation of the winding procedure*

For the design of the fiber layout a menu-controlled computer program ('**layout.m**') has been developed in MatLab 4.2 (*The MathWorks, Inc.*), which easily generates different layouts by varying a few parameters (Appendix A). This program produces cylindrical shaped fiber layouts designed by user-defined variables. The types of layouts can roughly be divided into unidirectional shapes, sinusoidal shapes or a combination of these shapes. The sinusoidal shapes can be subdivided into shapes with constant amplitudes, linear variable amplitudes or parabolic variable amplitudes. Design parameters like the number of fibers, the height and diameter of the cylinder, phase shifts and amplitude variation of sinusoidal layouts are used as input data to define the fiber layout. Manufacturing parameters such as the diameter of the winding cylinder, the distance of the winding eye to the winding cylinder and the revolution of the winding cylinder are used as input data. The geometric data of the layout is stored in two files with different formats. One format is used for numerical applications (chapter

4), whereas the other format is used to control the motors of the winding machine, i.e. a motor to rotate the winding cylinder and a motor for the translation of the winding eye. The combination of rotation and translation of these components results in a fiber layout over the stent conform with the actually designed layout (Fig 3.2 and 3.4). With this procedure versatile fiber layouts can be made giving the possibility to reinforce the composite material in the areas where the highest stresses occur. Typical layouts generated by this program are shown in Appendix A.

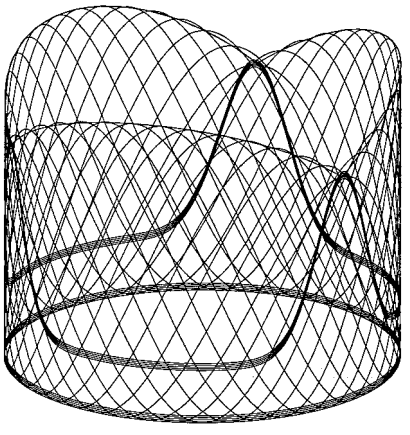

Figure 3.4: *Typical computer designed sinusoidal fiber layout*

After the winding procedure is finished, the mold is again dipped in the rubber solution to fully cover the fibers with rubber. This procedure can be repeated and in this way different fiber reinforced layers can be combined into a complex composite structure. Next, the mold is put in an oven to vulcanize the rubber (the crosslinker is activated by the temperature rise). The stiffness of the rubber can, within some limits, be adjusted with the oven temperature, the vulcanization time and the crosslinker quantity.

Followed by the crosslinking procedure, the valve stent combination is taken from the mold with the aid of soap suds. In this way an open, cylindrical shaped, stress-free valve is obtained (Fig. 3.2), which differs from the polyurethane valve or the porcine and pericardial valves which have a closed or half-closed stress-free position. Moreover, prostheses have been made with a closed stress-free configuration by keeping the valve closed in the oven for a certain time. It is observed that the opening and closing behaviour is strongly influenced by how the leaflets are kept closed, which is a hard to control production step. So, the behaviour of these leaflets was not reproducible and therefore, an open stress-free valve is produced, which has a good closing behaviour [4].

3.5 Experimental Methods

To test the valve prostheses, it is put in a circulation device, a so-called 'pulse duplicator', that imitates a physiological loading. A detailed description of this device is given in [4]. A schematic drawing of this system is shown in Fig. 3.5. The left ventricle is simulated by an air pressure controlled piston [4]. A constant supply pressure during the relaxation phase is obtained by means of a reservoir with an overflow. Behind the perspex housing with the

sinus of Valsalva cavities, in which different valve prostheses can be mounted, a compliance is connected to compensate for the rigidity of the housing and the flow meter, followed by the load impedance system. By measuring the pressure at the left ventricular and aortic side, the pressure gradient over the valve is obtained. Also the pressure directly behind the leaflet in the sinus cavity is measured. This is the same as the pressure measured a few millimeters away from the valve prototype (the aortic pressure), so this pressure can be used as a boundary condition in the numerical model (chapter 4). Moreover, the leakage of the valve, during valve closure, is measured. These measurements are done for both pulsatile and steady flows and the results can be found in [4].

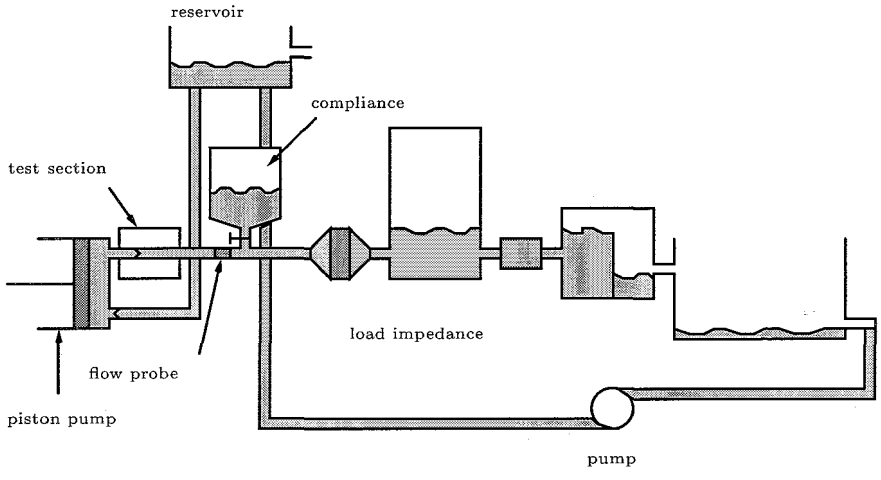

Figure 3.5: *Schematic presentation of the 'pulse duplicator'.*

In the next chapter a numerical model of this three-leaflet synthetic valve is presented and its implementation in the FEM package MARC is described. Geometric properties, material properties and the boundary conditions of this model will be described in detail. The algorithm used to solve this problem is also discussed with a few comments on the background of the solution algorithm.

Chapter 4

FEM Model of the Three-Leaflet Synthetic Valve Prosthesis

4.1 Introduction

The three-leaflet synthetic valve prosthesis, discussed in the previous chapter, is a prototype of an aortic heart valve prosthesis designed for better durability of mechanical and hemodynamic performance. The leaflets of the prototype consist of a fiber reinforced rubber matrix material enclosed by rubber layers (chapter 3, section 3.4). It is expected that decreasing stresses in the outer rubber layers of a leaflet will result in a decrease of tears and perforations in the central part of the leaflet and at the vicinity of the leaflet attachment and in a decrease of calcification of the leaflets. Changing the fiber reinforcement and investigating the effects on tissue failure experimentally would be too expensive and too time-consuming. Therefore, numerical simulations are performed to predict the behaviour of the experimental testing models under simulated physiological load. This chapter will describe a numerical model of the artificial fiber reinforced three-leaflet aortic valve with a rigid stent. Within this finite element model the geometric and material properties as well as the mechanical boundary conditions of the prosthesis will be taken as realistic as possible.

4.2 FEM Model Properties

4.2.1 Geometry and Mesh

The dimensions of the prosthesis are used as input data for the numerical model. Because the stent of the tested prostheses is relatively rigid it is not modeled and, therefore, the leaflet fixation to the stent is realized using boundary conditions at the fixation area (section 4.2.3).

The leaflets show a cylindrical shape with a diameter of 2 mm in the open, stress-free position (Fig. 3.2). The attachment of a leaflet to the stent in the prosthesis is modeled as a circular curved fixation of the leaflet to an 'imaginary' stent (Fig. 4.1). To the middle of the leaflet at the free edge (Fig. 2.3) the leaflet shows a semilunar shape. Because of this shape, the maximum height of the leaflet is 12.5 mm at the middle of the leaflet, and the minimum height is 10 mm at the commissure. Furthermore, the thickness of the leaflets of the prosthesis varies from 300 μm to 500 μm depending on the number of fibers and rubber layers. In the numerical model the thickness of the leaflet is taken uniform: 400 μm.

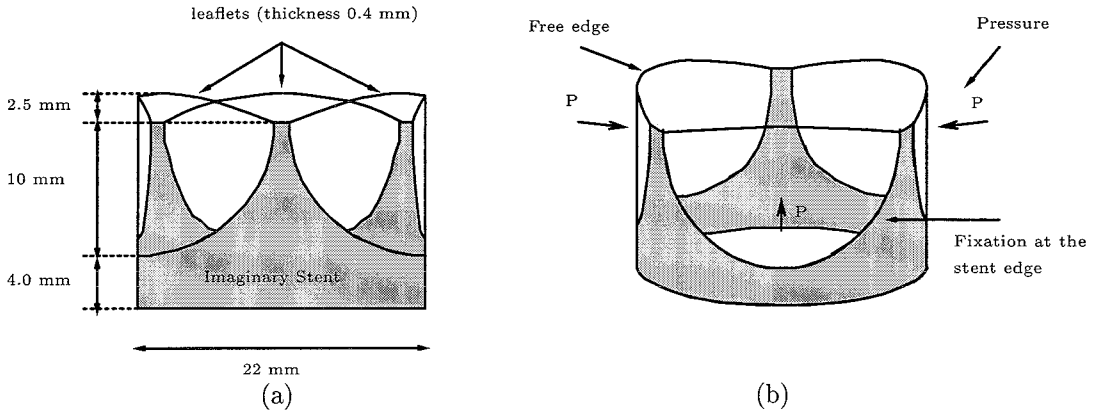

Figure 4.1: *(a) Front view of the model with dimensions. (b) The model from a different view point and the pressure load on the leaflets.*

For the implementation of this model in the FEM package MARC the pre-processor MENTAT II 3.1 is used. Because of the symmetry of the prosthesis only $\frac{1}{6}^{th}$ of the valve will be modeled. First, a surface is defined representing half of one leaflet. This surface is converted into a mesh consisting of 319 quadrilateral elements as shown in Fig. 4.2. To be able to include the bending stiffness of the leaflets, so-called shell elements are used in the model. Within MARC these elements are referred to as four-node thick shell elements with global displacements and rotations as degrees of freedom. A bilinear interpolation is used for the coordinates, displacements and rotations. The membrane strains are obtained from the displacement fields, the curvatures from the rotation field. The mechanical behaviour of such a shell element can be described by a relation between these membrane strains and curvatures on the one hand and in-plane forces and moments on the other [10]. From this relation, stresses and strains are calculated with respect to the material axes of the element $(\vec{v}_1, \vec{v}_2, \vec{v}_3)$.

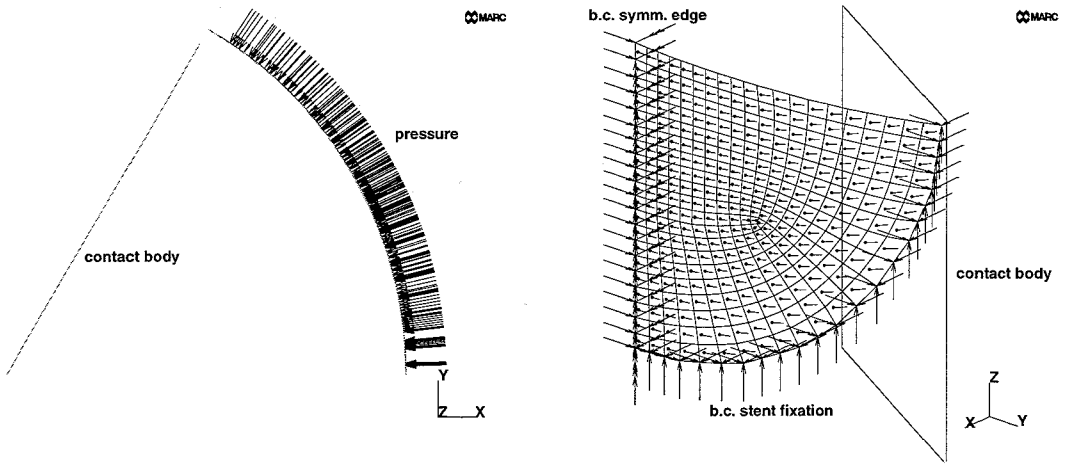

Figure 4.2: *(Left) Top view of the model with a pressure load on all elements. (Right) The model from a different view point with the fixation along the curved edge and symmetry edge. The —o in each element gives the direction of the first material axis of the element.*

The directions of those material axes are defined by a local coordinate system (Appendix B), which depends on the three-dimensional shape of the element and the connectivity of the four nodes. Since each element has a different shape (Fig. 4.2) and connectivity of nodes, the local element coordinate system differs from element to element. This results in a stress and strain output which is unable to interpret. Using the "ORIENTATION" option within MARC [14], equal directions can be given to the first material axes of all elements. The orientations of the second and third material axes of the elements are also defined with that. To get stresses in a user defined preferred direction subroutines can be used [16].

4.2.2 Implementation of Material Properties

As described in chapter 3 the leaflets have a composite structure, which is composed of two different materials, i.e. EPDM rubber and HP-PE fibers. The structure of this material is built up in the following way: a rubber top-layer, versatile PE fiber middle-layers embedded in a rubber matrix and a rubber bottom-layer (Fig. 4.3). The directions of the global coordinate system are denoted with $\vec{v}_x$, $\vec{v}_y$ and $\vec{v}_z$, whereas the directions $\vec{v}_1$, $\vec{v}_2$ and $\vec{v}_3$ represent the material directions in the material coordinate system.

In this model the leaflet layers are modeled as linear elastic materials. Being a thin and membrane like structure, a plane stress situation is assumed to exist in the leaflets. For the outer rubber layers of the composite structure a linear elastic, nearly incompressible, isotropic material model is used according to Hooke's law. With Young's modulus $E = E_m$ and Poisson's ratio $\nu = \nu_m$ (section 3.3.1) the stress-strain relation in these layers is:

$$\underbrace{\begin{bmatrix} \sigma_{11} \\ \sigma_{22} \\ \sigma_{12} \end{bmatrix}}_{\underline{\sigma}_r} = \underbrace{\frac{E}{1-\nu^2} \begin{bmatrix} 1 & \nu & 0 \\ \nu & 1 & 0 \\ 0 & 0 & (1-\nu) \end{bmatrix}}_{\underline{S}_r} \underbrace{\begin{bmatrix} \varepsilon_{11} \\ \varepsilon_{22} \\ \varepsilon_{12} \end{bmatrix}}_{\underline{\varepsilon}_r} \tag{4.1}$$

with symmetrical stiffness matrix $\underline{S}_r$. The middle layers of the composite, consisting of PE fiber structures embedded in rubber, are modeled as linear elastic orthotropic materials. Having a local longitudinal modulus E_{11}, a local transversal modulus E_{22}, a shear modulus

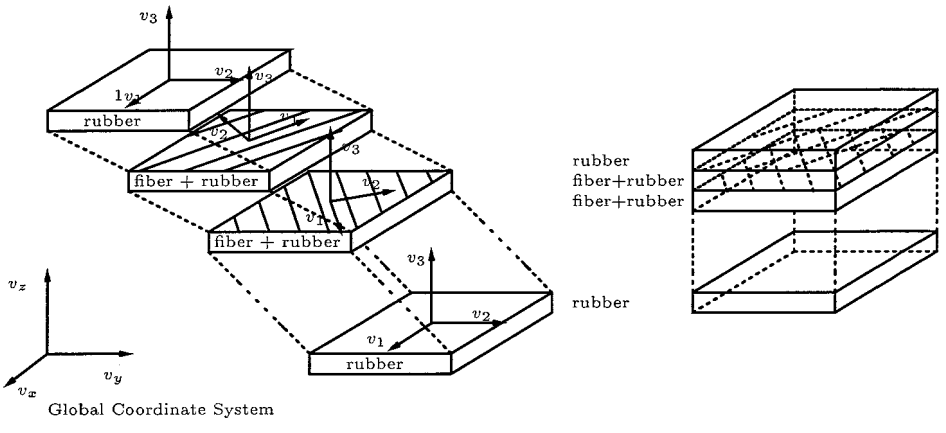

Figure 4.3: *Composite structure of the leaflet in the model.*

G_{12} and Poisson's ratio ν_{12}, the stress-strain relation in these layers in a plane stress situation with respect to the material coordinate system is:

$$\underbrace{\begin{bmatrix} \sigma_{11} \\ \sigma_{22} \\ \sigma_{12} \end{bmatrix}}_{\underline{\sigma}_f} = \underbrace{\frac{1}{1-\nu_{21}\nu_{12}} \begin{bmatrix} E_{11} & \nu_{21}E_{11} & 0 \\ \nu_{12}E_{22} & E_{22} & 0 \\ 0 & 0 & \frac{1}{2}(1-\nu_{21}\nu_{12})G_{12} \end{bmatrix}}_{\underline{S}_f} \underbrace{\begin{bmatrix} \varepsilon_{11} \\ \varepsilon_{22} \\ \varepsilon_{12} \end{bmatrix}}_{\underline{\varepsilon}_f} \tag{4.2}$$

with symmetrical stiffness matrix $\underline{S}_f$. According to Maxwell's equation, the relation between ν_{12} and ν_{21} is: $\frac{\nu_{12}}{E_{11}} = \frac{\nu_{21}}{E_{22}}$. The total stiffness matrix $\underline{S}$ of the complete composite structure is calculated from the contributions of $\underline{S}_r$ and $\underline{S}_f$ of the layers to the in-plane forces and moments [10]. In MARC such composite structures are implemented using the "COMPOSITE" option.

For complex fiber structures, like the sinusoidal fiber layout in Fig. 3.4, the material directions may locally be different. In the model these material directions are defined by the local coordinate system of the elements in the mesh (section 4.2.1). It is desired to define a general material coordinate system for all elements with respect to which the material properties of the fiber in the mesh can be defined. In this model the first material axis of each element is taken circumferential, parallel to the x-y-plane of the global coordinate system (Fig 4.2). The second material axis is perpendicular to the first material axis and both material axes are situated in the tangent plane at the centroid of the element (Appendix B). So, the composite properties of each element depend on the fiber layout and the orientation of the material axes of the element in the mesh. This can easily be understood from Fig. 4.4.

In Fig. 4.4(b) a two-dimensional representation of the mesh is given with a sinusoidal fiber layout. It is clear that for each element the number of fibers crossing is different. Elements without any fiber have thickness 0.4 mm and have the material property of the EPDM rubber. These elements are not shown in this figure. All other elements have the property of a composite, which is built up of two outer isotropic rubber layers enclosing a varying number of orthotropic fiber layers embedded in a rubber matrix with thickness equal to the diameter of the fiber (0.06 mm). Each orthotropic layer of a specific element represents one fiber that crosses that element. Consider, for example, a specific element as shown in Fig. 4.4b. There are two fibers crossing this element so, two orthotropic layers are defined.

A computer program ('**profib.m**') has been developed in MatLab 4.2 (*The MathWorks, Inc.*) for the implementation of computer designed fiber layouts in the numerical model. The procedure of this implementation is as follows:

1. A data-file of the numerical model (MENTAT II) and a file with the geometric data of the fiber layout is generated. These files, together with the thickness of the elements and the diameter of the PE fibers, are used as input for the computer program '**profib.m**'.

2. The computer program analyses these files and determines the geometric position of the nodes of each element and each fiber of the layout with respect to a global coordinate system.

3. For each fiber the intersection points with the edges of an element are calculated ('o' in Fig. 4.4(b)). The connection line between the intersection points associated with a certain fiber represents the part of that specific fiber that is in the element.

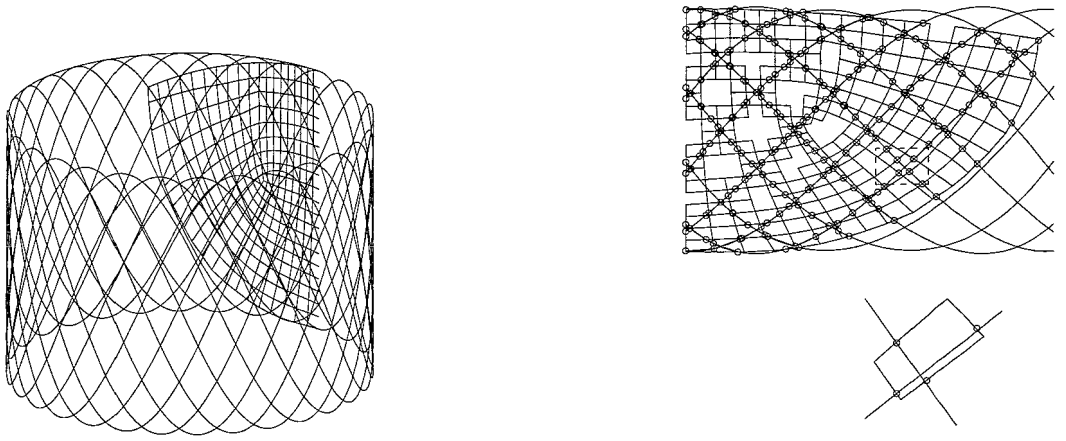

(a) (b)

Figure 4.4: *(a) 3-D view of the generated fiber layout and the mesh of the numerical model. (b) 2-D view of the numerical model and the fiber layout.*

For this fiber part an equivalent orthotropic layer is defined as a homogeneous continuum of both fiber material and rubber material. The thickness of this layer is equal to the diameter of the fiber and the surface is equal to the element surface.

4. The volume fractions of the fiber part and the rubber matrix with respect to the total volume of the defined orthotropic layer are calculated. From these volume fractions material parameters for the orthotropic layer are determined with the Halpin-Tsai equations [9] for a plane stress situation.

5. Three composite parameters are defined for this layer: a) a material identification referring to the material properties determined in step 4; b) the relative thickness of this layer to the total element thickness; c) the ply-angle α of this layer with respect to the orientation of the first material axis ("ORIENTATION").

Step 4 and 5 are repeated for each fiber that crosses the element. For each fiber part in the element a new orthotropic layer is defined with new composite parameters, which is placed on top of the previous defined orthotropic layer.

6. Two isotropic layers are defined, with the material property of the rubber (section 3.3.1), to enclose the orthotropic layer(s). The thicknesses of these layers are equal to half of the total element thickness minus the thickness(es) of the orthotropic layer(s).

7. Step 3 to 6 is repeated for each element of the mesh. The information obtained for each composite layer of each element is written to a 'procedure' file using a format that is accessible for MENTAT II.

8. The 'procedure' file is executed within MENTAT II on a model with isotropic material properties of rubber for all elements. For elements that are crossed by fibers these material properties are automatically replaced by composite properties representing the original leaflet composite structure.

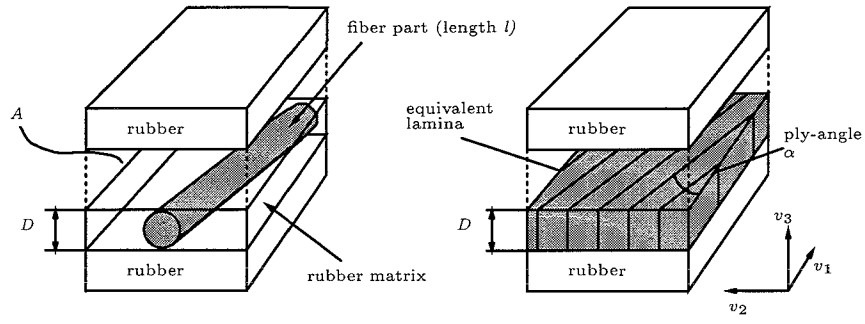

Figure 4.5: *Material model of the leaflet composite structure.*

For the determination of the orthotropic material parameters (step 4) a composite material model is used as shown in Fig. 4.5. On the left side a lamina is shown with a fiber part embedded in a rubber matrix. The volume of the fiber part is $V_f = \frac{1}{4} \times D^2 \times \pi \times l$ with D the diameter and l the length of the fiber part. Consider the surface A of this lamina to be equal to the surface of an element calculated from the coordinates of the four nodes. The total volume of the lamina with the fiber part then is $V_t = A \times D$. Consequently, the volume fraction of this fiber part in this lamina is

$$v_f = \frac{V_f}{V_t} \tag{4.3}$$

Thus the volume fraction of the rubber matrix with volume V_m in this lamina is

$$v_m = \frac{V_m}{V_t} \qquad \text{or} \qquad v_m = (1 - v_f) \tag{4.4}$$

With these volume fractions and the Halpin-Tsai equations the material parameters E_{11}, E_{22}, G_{12} and ν_{12} of the stress-strain relation (4.2) can be determined [9]:

$$E_{11} \cong E_f v_f + E_m v_m \tag{4.5}$$

and

$$\nu_{12} \cong \nu_f v_f + \nu_m v_m \tag{4.6}$$

and

$$\frac{\hat{p}}{p_m} = \frac{(1 + \zeta \eta v_f)}{(1 - \eta v_f)} \tag{4.7}$$

where

$$\eta = (p_f/p_m - 1)/(p_f/p_m + \zeta) \tag{4.8}$$

In this formulation the quantities $\hat{p}$, p_f, p_m and ζ are identified as:

$\hat{p}$ = composite moduli, E_{22}, G_{12}
p_f = corresponding fiber modulus, E_f, G_f, v_f respectively
p_m = corresponding matrix modulus, E_m, G_m, v_m
ζ = a measure of reinforcement

The quantities of p_f and p_m were earlier given in section 3.3.1.

As stated in [9] reliable estimates for the ζ factor can be obtained by comparison of eq. (4.7) and (4.8) with numerical micromechanics solutions employing formal elasticity theory. For this model $\zeta = 1$ and $\zeta = 2$ are appropriate values for the prediction of shear G_{12} and stiffness E_{22} respectively [9].

4.2.3 Implementation of Boundary Conditions

The mechanical boundary conditions of the prosthesis are defined by the fixation to the stent and by fluid motion in the pulse duplicator or, for in vivo situations, in the aorta. However, no fluid interactions are taken into account, since they are too difficult to model at the present time. Deformation is realized by applying a pressure on the leaflet. Therefore, the boundary conditions of the current model are only of a quasi-static mechanical character. There are in fact three different types of boundary conditions: fixed displacement conditions, contact conditions and mechanical load conditions.

Along the stent edge, movement of the leaflet is suppressed in all directions. With modeling only $\frac{1}{6}^{th}$ of the total prosthesis, i.e. half of one leaflet, an additional fixation condition is requested for the nodes on the symmetry axis of the leaflet. Only displacements in the x-direction and z-direction and free rotation along the y-axis of the global coordinate system is allowed for these nodes (Fig. 4.2). In this way, the leaflet is at the symmetrical edge always perpendicular to the global z-x-plane.

An other type of boundary condition is caused by the coaptation area of the leaflets. When moving inwards, the leaflets come in contact with each other, resulting in a restriction of the movement of the leaflets in this direction. In the numerical model this is realized by using a contact body which represents the coaptation area of the leaflets. This contact body is rigid and has a fixed position. Within some distance ($\frac{1}{2}$ of the thickness of the shell element) the nodes of the mesh are considered to be in contact with this body. More information about the contact algorithms can be found in [15].

The closing and opening deformations of the leaflets are identical, since linear elastic behaviour is modeled. So, with analyzing only the closing (or only the opening) of the leaflets, all relevant information about the mechanical character of the numerical model is obtained. Therefore, only a pressure load, as measured from the pressure difference between aorta and ventricular side with a maximum of 12 kPa (Fig. 2.6), is applied at the leaflet surface causing the leaflets to move from an open stress-free position inwards to the center of the model (Fig. 4.1). In the numerical model pressure is realized with a following face load applied to all elements using the "FOLLOW FOR" option in MARC. In this way, a mechanical load is applied that resembles the physiological load of the prosthesis as far as possible. However, from a physiological point of view, it is incorrect to realize deformation of the model with a pressure load that is uniform over the leaflets and measured at positions away from the leaflets (chapter 3). Movement of the leaflets is primarily caused by the complex fluid flow that causes (probably) non-uniform pressures and shear stresses on both sides of the leaflets.

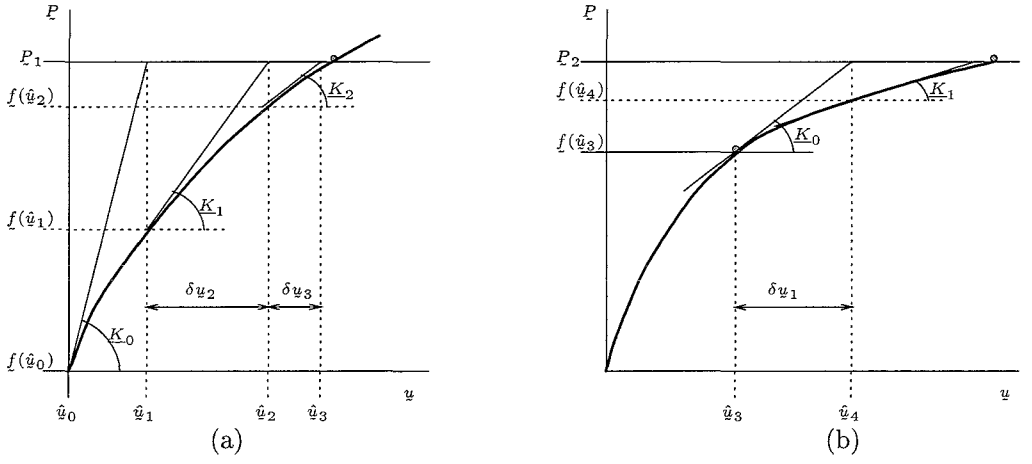

Figure 4.6: *'Full Newton-Raphson' iterative procedure; (a) first load step, (b) second load step.*

4.3 Numerical Solution Control

4.3.1 Introduction

The numerical model is formulated using the 'Updated Lagrangian' ("UPDATE") approach, which means that the element stiffness matrix is assembled in the current configuration of the element and, that the stress and strain outputs are given with respect to the coordinate system in the updated configuration of the element. Geometric non-linearities due to large displacements and large rotation effects are included using standard procedures in MARC ("LARGE DISP"); the same applies for any non-linearity in the loading or boundary conditions.

A combination of the 'Full Newton-Raphson' iterative procedure and a 'Path-Following' algorithm, is used to solve the numerical model. First, the 'Full Newton-Raphson' iterative procedure is described. With this procedure a system of non-linear equilibrium equations can be solved proceeding from a known solution to an adjacent configuration. However, the numerical model shows many elastic instabilities during the deformation of the leaflets. To illustrate the character of the deformation of the leaflets some elementary elastic instability problems are shown in subsection 4.3.3. 'Path-Following' solution methods are required to solve such problems numerically. The basis of this solution method is briefly discussed in subsection 4.3.4.

4.3.2 The 'Full Newton-Raphson' Iterative Procedure

The load stepping procedure which is used to solve the numerical model is basically an incremental procedure to apply the total load $\underset{\sim}{P}$ on the model and solve the associated model displacements $\underset{\sim}{u}$ from the (non-linear) model equilibrium

$$\underset{\sim}{f}(\underset{\sim}{u}) = \underset{\sim}{P} \tag{4.9}$$

with $\underset{\sim}{f}$ the internal forces. Iterative methods must be used to solve the non-linear equation (4.9). Usually the equilibrium path is followed incrementally proceeding from a known solution to an adjacent configuration. The 'Full Newton-Raphson' iterative procedure, illustrated in Fig. 4.6, is used to solve this problem.

The first incremental load step is $\underset{\sim}{P}_1$ and the solution is iteratively obtained until convergence is reached, as illustrated below:

$$\begin{array}{l}
\textbf{increment } n = 1 \quad \rightarrow \quad \underset{\sim}{P}_1 \text{ (Fig. 4.6(a))} \\
\textbf{iteration} \quad i = 1 \\
\quad \underline{K}_0 \cdot \delta\underset{\sim}{u}_1 = \underset{\sim}{P}_1 - \underset{\sim}{f}(\hat{\underset{\sim}{u}}_0) \quad \rightarrow \quad \delta\underset{\sim}{u}_1 \quad \rightarrow \quad \hat{\underset{\sim}{u}}_1 = \hat{\underset{\sim}{u}}_0 + \delta\underset{\sim}{u}_1 \\
\quad \text{no convergence} \quad \rightarrow \quad \textbf{iteration } i = 2 \\
\quad \underline{K}_1 \cdot \delta\underset{\sim}{u}_2 = \underset{\sim}{P}_1 - \underset{\sim}{f}(\hat{\underset{\sim}{u}}_1) \quad \rightarrow \quad \delta\underset{\sim}{u}_2 \quad \rightarrow \quad \hat{\underset{\sim}{u}}_2 = \hat{\underset{\sim}{u}}_1 + \delta\underset{\sim}{u}_2 \\
\quad \text{no convergence} \quad \rightarrow \quad \textbf{iteration } i = 3 \\
\quad \underline{K}_2 \cdot \delta\underset{\sim}{u}_3 = \underset{\sim}{P}_1 - \underset{\sim}{f}(\hat{\underset{\sim}{u}}_2) \quad \rightarrow \quad \delta\underset{\sim}{u}_3 \quad \rightarrow \quad \hat{\underset{\sim}{u}}_3 = \hat{\underset{\sim}{u}}_2 + \delta\underset{\sim}{u}_3 \\
\quad \text{convergence} \quad \rightarrow \quad \underset{\sim}{u}_3 = \hat{\underset{\sim}{u}}_3
\end{array} \tag{4.10}$$

$$\begin{array}{l}
\textbf{increment } n = 2 \quad \rightarrow \quad \underset{\sim}{P}_2 \text{ (Fig. 4.6(b))} \\
\textbf{iteration} \quad i = 1 \\
\quad \underline{K}_0 \cdot \delta\underset{\sim}{u}_1 = \underset{\sim}{P}_2 - \underset{\sim}{f}(\hat{\underset{\sim}{u}}_3) \quad \rightarrow \quad \textit{etc.}
\end{array} \tag{4.11}$$

In general, the solution procedure for such load stepping algorithms for step n and iteration i is:

$$\begin{array}{ll}
\textbf{SOLVE} & \underline{K}_{i-1} \cdot \delta\underset{\sim}{u}_i = \underset{\sim}{P}_n - \underset{\sim}{f}(\hat{\underset{\sim}{u}}_{i-1}) \\
\textbf{UPDATE} & \hat{\underset{\sim}{u}}_i = \hat{\underset{\sim}{u}}_{i-1} + \delta\underset{\sim}{u}_i
\end{array} \tag{4.12}$$

with $\hat{\underset{\sim}{u}}_i$ and $\hat{\underset{\sim}{u}}_{i-1}$ as best estimates for the exact solution of displacements in two subsequent iterations.

The procedure for convergent criteria is based on the magnitude of the maximum residual forces compared to the maximum reaction forces. The residual forces are defined as the difference between the applied load step and the calculated internal forces. This method is appropriate since the residuals are a measure of the out-of-equilibrium forces, which should be minimized. This residual checking procedure is outlined below:

$$\frac{\|\underset{\sim}{F}_{residual}\|_{max}}{\|\underset{\sim}{F}_{reaction}\|_{max}} < TOL_1 \qquad \text{and} \qquad \frac{\|\underset{\sim}{M}_{residual}\|_{max}}{\|\underset{\sim}{M}_{reaction}\|_{max}} < TOL_2 \tag{4.13}$$

where $\underset{\sim}{F}$ is the force vector and $\underset{\sim}{M}$ is the moment vector. TOL_1 and TOL_2 are control tolerances and are in this numerical model both set to 0.01. $\|\underset{\sim}{F}\|_{max}$ indicates the component of $\underset{\sim}{F}$ with highest absolute value.

With this iterative solution procedure ordinary non-linear systems can be solved. In the next subsection, however, some elementary non-linear instability problems will be discussed that require more sophisticated solution algorithms. These elementary instability problems represent the character of deformation of the numerical model.

4.3.3 Elastic Instability Problems

The numerical model, as described in section 4.2, is relatively simple from a modeling point of view. However, the structure is mechanically complex showing instabilities when under load.

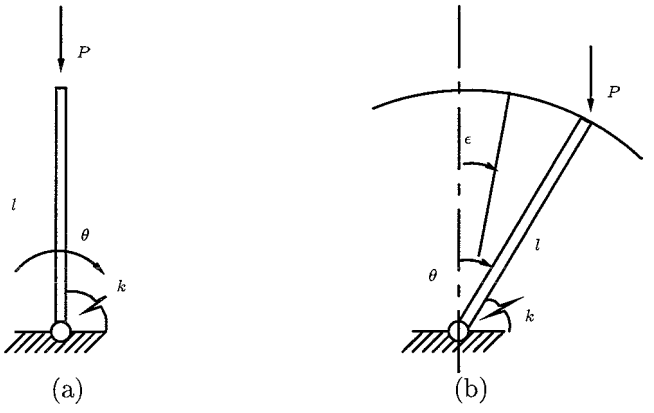

Figure 4.7: *Hinged cantilever: (a) undeflected perfect system; (b) deflected imperfect system [24].*

To illustrate the difficulties of these instability phenomena, simple structures that enclose these fundamental mechanical problems of the leaflet structure of the numerical model will be discussed in this subsection. A brief review is given based on examples found in the literature [22], [24], [25].

Example 1 Consider a rigid bar of length l, hinged at one end, free at the other, and supported by a linear rotational spring of stiffness k (Fig. 4.7(a)). The free end is loaded with a force P in the direction of the bar. The system is perfect in the sense that the spring is unstrained when the bar is vertical. The subsequent rotation of the bar is denoted by θ [24].

The equilibrium states of this system are given in Fig. 4.8(a). One equilibrium path (Fig. 4.8(a) (1)), the trivial *fundamental* path, is coincident with the load axis while a second (post-buckling) non-linear equilibrium path (Fig. 4.8(a) (2)) is intersecting the fundamental path at a critical equilibrium state C, which is referred to as a bifurcation point. A stability study of these equilibrium paths results in an unstable equilibrium for the fundamental path (1) beyond point C (broken line) and a stable equilibrium in all other cases (solid lines).

Suppose now that the system is imperfect in the sense that the rotational spring is unstrained when the link has a small rotation denoted by ϵ (Fig. 4.7(b)). Fig. 4.8(b) summarizes

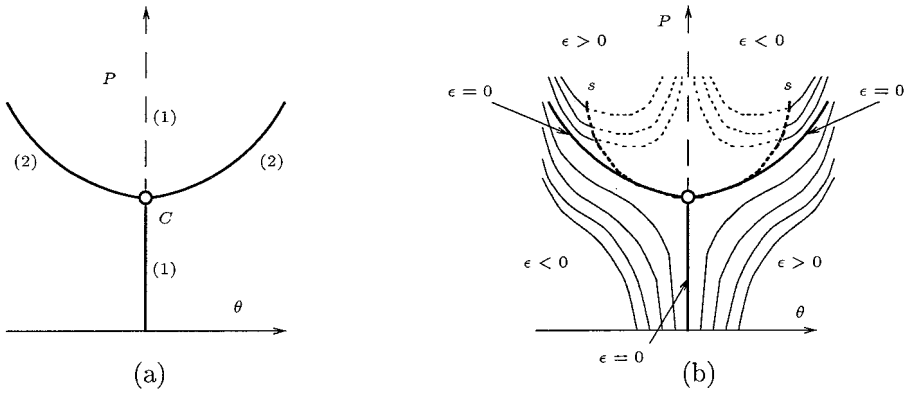

Figure 4.8: *Equilibrium paths of the perfect (a) and imperfect (b) systems [24].*

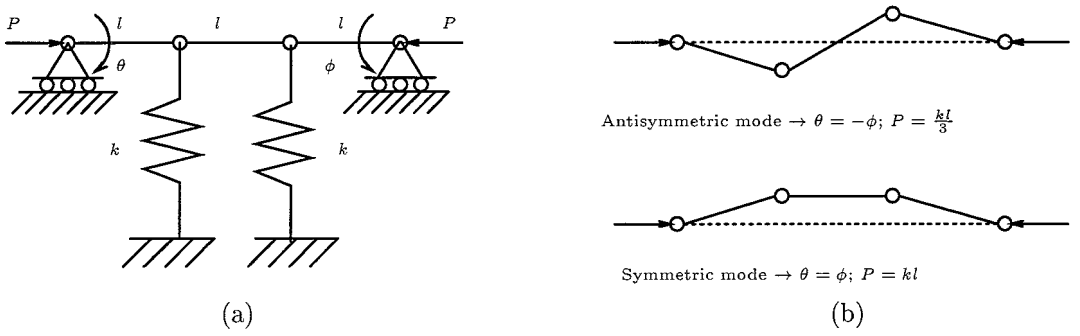

Figure 4.9: *Two-hinged system showing (a) the geometry and (b) the mode shapes [22].*

the responses of the family of systems. The locus of critical equilibrium states (curve ss) separates the stable and unstable domains [24].

Example 2 A two-degree-of-freedom system is composed of three rigid bars of length l hinged together as shown in Fig 4.9(a). The two linear springs have an equal stiffness k. A horizontal force P is applied to the system at the end of the two outer rigid bars.

Besides the trivial equilibrium state, which is coinciding with the load axis, two non-trivial equilibrium states are present as shown in Fig. 4.9(b). Study of the stability of the non-linear equilibrium positions characterized by $\theta = \phi = 0$ for the entire range of values for P results in an bifurcation point, which separates the stable from the unstable equilibrium positions [22].

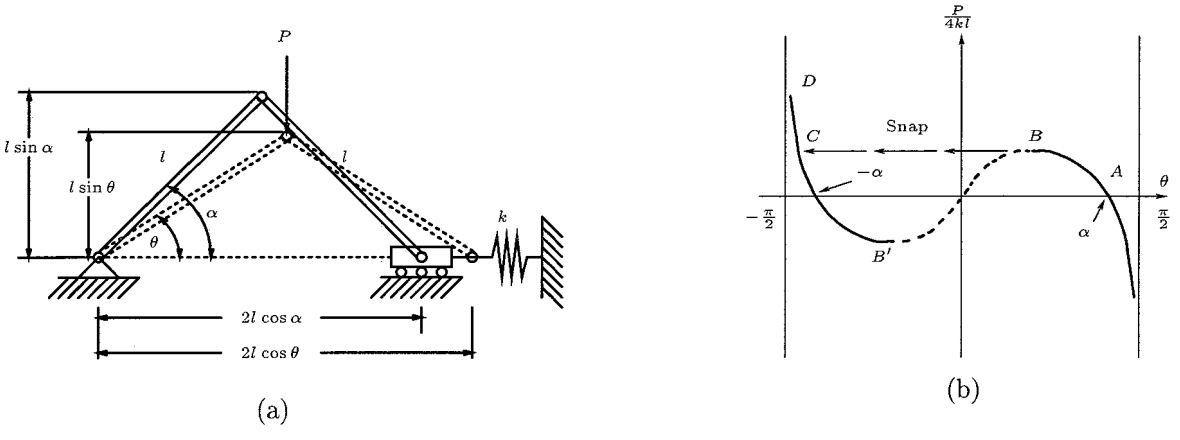

Figure 4.10: *(a) Geometry of the snap-through model (b) Load-deflection curve [22].*

Example 3 Consider two rigid bars of length l pinned together, with one end of the system pinned to an immovable support, and the other pinned to a linear horizontal spring (Fig. 4.10(a)). The rigid bars make an angle α with the horizontal when the string is unstretched and the system is loaded laterally through a force P applied at the connection of the two rigid bars. The question arises whether it is possible for the system to snap-through toward the other side ($\theta < 0$) at some value of the applied load [22].

The equilibrium states of this system are plotted in Fig 4.10(b). From a stability study

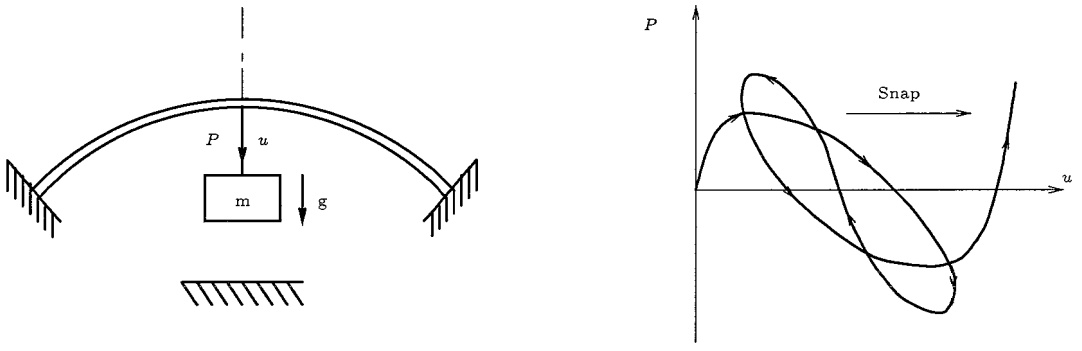

Figure 4.11: *(Left) Geometry of the structure; (Right) Load-deflection curve of the symmetric arch [22].*

the distinction between stable (solid line in Fig. 4.10(b)) and unstable equilibrium positions (broken line in Fig. 4.10(b)) is made [22]. The loading starts at point A and, as the load increases, it will reach point B, which is referred to as a bifurcation point. When point B is reached, the system will tend to snap-through toward the CD portion of the curve with no appreciable change in the load. The region BB' of the equilibrium path is never encountered in a normal loading sequence, but the equilibrium states do of course exist and can be observed if some element of control is introduced. In Fig. 4.11 such a response is illustrated for a vertical loaded arch, which is constrained to remain symmetrical about its vertical center-line. Because of this constraint the structure is forced to take a more complex equilibrium path, as shown with the load-deflection curve of this structure [25].

The fundamental problems discussed above can become very complex by simply adding an extra degree of freedom, resulting in more (un)stable equilibrium conditions (Example 2), or changing the conditions of the applied load (Example 3), whereas adding imperfections to a system may eliminate its unstable character (Example 1). Many bifurcation points and unstable equilibrium positions may occur in complex structures that enclose these elementary problems. In the numerical model of the three-leaflet aortic valve prosthesis these phenomena are present locally all over the valve. Large deformations lead to non-linear equilibrium paths, whereas two other sources, i.e. contact and follower force properties (section 4.2.3), increase the non-linear character of the numerical model.

The instability and non-linear problems are essential when solving the model, described in section 4.2, numerically. Well defined solution algorithms are necessary to solve this problem, because the 'Full Newton-Raphson' solution procedure may be deficient. The next section will describe the solution control in MARC that is used for this numerical model with these typical mechanical properties. 'Path-Following' algorithms in combination with the 'Full Newton-Raphson' iterative procedure are discussed to pass local unstable (bifurcation) points.

4.3.4 The 'Path-Following' Solution Algorithm

Within the iterative solution procedure described in subsection 4.3.2 a 'Path-Following' algorithm is used to control the load stepping of the numerical model. This implies that the total load step is subdivided into incremental steps with a partial load of the total load step, determined by the 'Path-Following' algorithm. The basis of this 'Path-Following' method is described briefly below. More information about this procedure can be found in [11], [6].

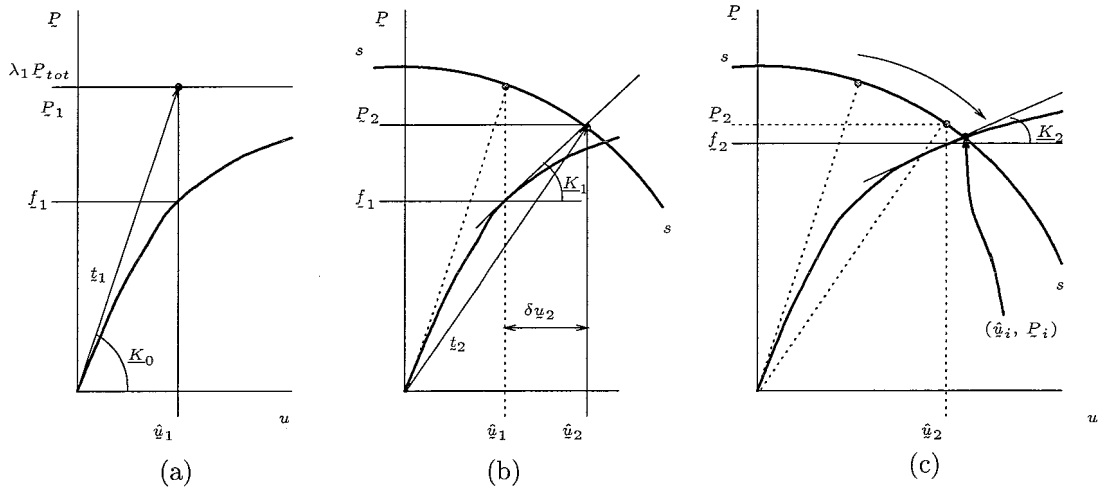

Figure 4.12: *The 'Path-Following' algorithm for subsequent iterations (a), (b) and (c).*

According to Chrisfield [6] the incremental load step is defined as: $\underset{\sim}{P}_n = \lambda_n \underset{\sim}{P}_{tot}$, with $\underset{\sim}{P}_n$ the current load, λ_n a load parameter and $\underset{\sim}{P}_{tot}$ the total applied load. Initially, at the beginning of the first increment, a load $\underset{\sim}{P}_1$ is defined from $\underset{\sim}{P}_1 = \lambda_1 \underset{\sim}{P}_{tot}$, with λ_1 the part of the total load allowed in this first step given by the user (Fig. 4.12(a)). With this load and the initial tangential stiffness matrix $\underline{K}_0$ the associated displacement vector $\delta \underset{\sim}{u}_1$ is determined from

$$\underline{K}_0 \delta \underset{\sim}{u}_1 = \underset{\sim}{P}_1 \qquad \text{or} \qquad \delta \underset{\sim}{u}_1 = \underline{K}_0^{-1} \underset{\sim}{P}_1 \tag{4.14}$$

The iterative displacement change $\delta \underset{\sim}{u}_1$ in this first iteration is equal to the incremental displacement $\Delta \underset{\sim}{u}_1$. The internal force vector associated with this configuration is denoted with $\underset{\sim}{f}_1$. From this configuration a vector $\underset{\sim}{t}_1^T = [\Delta \underset{\sim}{u}_1 \; \underset{\sim}{P}_1]$ is determined as shown in Fig. 4.12(a).

A new numerical parameter is introduced to determine the arc on which a new solution is to be found, i.e. the arc-length C. This arc-length C between two adjacent configurations is defined from vector $\underset{\sim}{t}_1$ as:

$$(C)^2 = \underset{\sim}{t}_1^T \cdot \underset{\sim}{t}_1 = \begin{bmatrix} \hat{\underset{\sim}{u}}_1^T & \underset{\sim}{P}_1^T \end{bmatrix} \cdot \begin{bmatrix} \hat{\underset{\sim}{u}}_1 \\ \underset{\sim}{P}_1 \end{bmatrix} = (\hat{\underset{\sim}{u}}_1)^2 + (\underset{\sim}{P}_1)^2 \tag{4.15}$$

with $C = constant$ in this increment. From the configuration $(\hat{\underset{\sim}{u}}_1, \underset{\sim}{P}_1)$ a new configuration $(\hat{\underset{\sim}{u}}_2, \underset{\sim}{P}_2)$, with $\underset{\sim}{P}_2 = \lambda_2 \underset{\sim}{P}_{tot}$, is being determined from

$$\underline{K}_1 \delta \underset{\sim}{u}_2 = \lambda_2 \underset{\sim}{P}_{tot} - \underset{\sim}{f}_1 \tag{4.16}$$

with $\underline{K}_1$ the current tangential stiffness matrix, λ_2 the current, unknown, load parameter and $\delta \underset{\sim}{u}_2$ the unknown iterative displacement change. The iterative displacement change $\delta \underset{\sim}{u}_2$ can, with λ_2 and $\delta \underset{\sim}{u}_2$ as unknown parameters, thus be written as:

$$\delta \underset{\sim}{u}_2 = \underline{K}_1^{-1} \lambda_2 \underset{\sim}{P}_{tot} - \underline{K}_1^{-1} \underset{\sim}{f}_1 \tag{4.17}$$

If $\hat{\underset{\sim}{u}}_2$ equals $\hat{\underset{\sim}{u}}_1 + \delta \underset{\sim}{u}_2$ (and $\underset{\sim}{P}_2$ equals $\lambda_2 \underset{\sim}{P}_{tot}$) a new, yet unknown, vector $\underset{\sim}{t}_2^T = [\hat{\underset{\sim}{u}}_2 \; \underset{\sim}{P}_2]$ can

be defined. Replacing vector $\underset{\sim}{t}_1$ of eq. (4.15) with vector $\underset{\sim}{t}_2$ the next equation arises:

$$(C)^2 = (\underset{\sim}{\hat{u}}_2)^2 + (\underset{\sim}{P}_2)^2 \tag{4.18}$$

or,

$$(C)^2 = (\underset{\sim}{\hat{u}}_1 + \delta\underset{\sim}{u}_2)^2 + \lambda_2^2 \underset{\sim}{P}_{tot}^2 \tag{4.19}$$

with C from eq. (4.15). In combination with eq. (4.17) this will result in

$$(C)^2 = (\underset{\sim}{\hat{u}}_1 + \underline{K}_1^{-1}\lambda_2 \underset{\sim}{P}_{tot} - \underline{K}_1^{-1}\underset{\sim}{f}_1)^2 + \lambda_2^2 \underset{\sim}{P}_{tot}^2 \tag{4.20}$$

which is a quadratic equation of the form

$$\alpha_1\lambda_2^2 + \alpha_2\lambda_2 + \alpha_3 = 0 \tag{4.21}$$

with,

$$\begin{aligned}
\alpha_1 &= (\underline{K}_1^{-1}\underset{\sim}{P}_{tot})^2 + \underset{\sim}{P}_{tot}^2 \\
\alpha_2 &= 2(\underline{K}_1^{-1}\underset{\sim}{P}_{tot})^T(\underset{\sim}{\hat{u}}_1 - \underline{K}_1^{-1}\underset{\sim}{f}_1) \\
\alpha_3 &= (\underset{\sim}{\hat{u}}_1 - \underline{K}_1^{-1}\underset{\sim}{f}_1)^2 - (C)^2
\end{aligned}$$

Equation (4.21) is referred to as the (spherical) constraint equation from which in general two solutions for the load parameter λ_2 are calculated. For one solution the iterative displacement change $\delta\underset{\sim}{u}_2$ is determined as:

$$\delta\underset{\sim}{u}_2 = \underline{K}_1^{-1}(\lambda_2 \underset{\sim}{P}_{tot} - \underset{\sim}{f}_1) \tag{4.22}$$

The choice of the solution of the quadratic equation (4.21) for iteration i is determined from $\underset{\sim}{\hat{u}}_{i+1} \cdot \underset{\sim}{\hat{u}}_i = \left\|\underset{\sim}{\hat{u}}_{i+1}\right\| \cdot \|\underset{\sim}{\hat{u}}_i\| \cos\theta$, which is solved for both λ's. In this equation θ is the angle between two adjacent displacement vectors. If the solution results in one positive and one negative value, the positive value is used. If the solution results in both values positive, the largest positive value is used. For the situation of both values negative, the solution should be checked on the displacement contribution of the residual force vector and this contribution should be reduced, changing numerical control parameters.

At this stage the configuration ($\underset{\sim}{\hat{u}}_2$, $\underset{\sim}{P}_2$) is known, which is on the arc ss of Fig. 4.12(b). Again, a new configuration ($\underset{\sim}{\hat{u}}_3$, $\underset{\sim}{P}_3$) is being determined, solving eq. (4.16) to (4.22) with a new tangential stiffness matrix $\underline{K}_2$ and a new internal force vector $\underset{\sim}{f}_2$. This iterative procedure repeats until configuration ($\underset{\sim}{\hat{u}}_i$, $\underset{\sim}{P}_i$) of Fig. 4.12(c) is reached, which is within a user-defined tolerance area of the exact solution, i.e. the intersection of the arc ss and the system equilibrium path. The best estimate for the exact solution of the total displacement vector of the first increment, after iteration i, is $\underset{\sim}{\hat{u}}_i = \underset{\sim}{\hat{u}}_{i-1} + \delta\underset{\sim}{u}_i$, which is associated with the incremental load step $\underset{\sim}{P}_i$.

From this converged configuration a new increment starts with a modified arc-length C, which is dependent of the arc-length of the previous increment, the number of iterations of the previous increment and the desired number of cycles in an increment, provided by the user. Initially, the load of this new increment is dependent of the load of the last iteration in the previous increment. The solution procedure of the 'Path-Following' algorithm discussed above repeats until convergence is reached at increment n for the total applied load $\underset{\sim}{P}_{tot}$.

The numerical model of the three-leaflet aortic valve prosthesis is solved using 'Path-Following' algorithms in MARC ("AUTO INCREMENT"). The standard procedure is basically as discussed above, however, the load contribution of iteration i, i.e $\lambda_i^2 \underset{\sim}{P}_{tot}^2$, to eq. (4.20) is left out. So, eq. (4.20) is reduced to

$$(C)^2 = (\underset{\sim}{\hat{u}}_{i-1} + \underline{K}_{i-1}^{-1} \lambda_i \underset{\sim}{P}_{tot} - \underline{K}_{i-1}^{-1} \underset{\sim}{f}_{i-1})^2 \tag{4.23}$$

and is referred to as the constraint equation, which is solved for λ_i. The proceedings of the "AUTO INCREMENT" solution algorithm are as discussed above. The results, which are obtained from solving the numerical model with the discussed solution algorithms, are presented in the next chapter.

Chapter 5

Results

5.1 Introduction

In this chapter results of the numerical model, as described in chapter 4, section 4.2, are discussed. Numerical simulations are performed of experimental tensile and bending tests of leaflet material structures. From these simulations confidence is gained about the modeling of leaflet material structures and their deforming behaviour (section 5.2). In section 5.3 solution problems are discussed that occurred solving the numerical model in some cases of fiber reinforcement. To be able to analyze the model for any particular fiber reinforcement adjustments for the fiber modulus and the pressure load are introduced in the model. The effect of the fiber modulus on model responses is discussed in section 5.4. Moreover, the results of a model without any fiber reinforcement are compared to corresponding results found in the literature. The responses of some fiber reinforced models are presented for the full closed valve and the half closed valve.

5.2 Numerical Verifications of the Leaflet Material Modeling

Since stresses over the aortic valve prosthesis cannot be measured experimentally at the present time and, since fiber reinforced valve models have not been developed before, verification of numerical results obtained from the model of the three-leaflet aortic valve prosthesis is difficult. Therefore, simple experiments with fiber reinforced leaflet matrix materials are performed. These experiments are simulated numerically and results are compared.

Tensile tests are performed with the 'Zwick' tensile testing machine on PE fiber reinforced EPDM rubber samples. Because of the large difference in stiffness between the PE fibers and the EPDM rubber, rectangular shaped samples may show wrinkling when clenched in the tensile testing machine. Therefore, tensile tests have been performed on tube shaped samples as shown in Fig. 5.1(a) and (b). The samples are clamped between two rings (Fig. 5.2(a)), which are fixed to fixing jaws. The upper jaw remains in position, whereas the other jaw moves down with a rate of stretch for both samples of 5 mm/min, which should be low enough to prevent viscoelastic effects. High strain levels were not reached, so there was no permanent deformation.

Two identical tests are performed for two different fiber reinforcements. The first sample (sample 1) has a unidirectional circumferential oriented reinforcement of 17 fibers (Fig. 5.1(a)), whereas the second sample (sample 2) has a sinus shaped reinforcement of 15 fibers

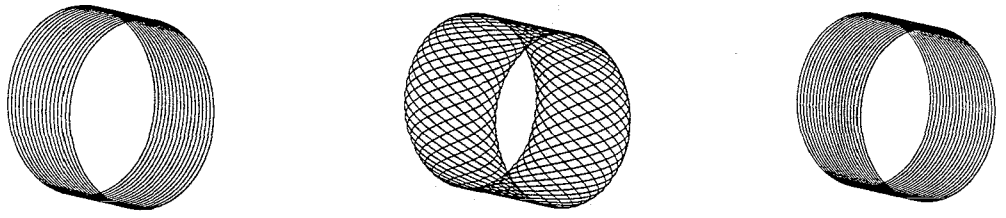

(a) sample 1 (b) sample 2 (c) sample 3

Figure 5.1: *Tube shaped samples used for tensile tests ((a) and (b)) and bending tests ((c)).*

(Fig. 5.1(b)). The Young's modulus in the direction of the loading, i.e. perpendicular to the tube axis, is measured of sample 1 between strains of 1% and 3% and of sample 2 between strains of 4% and 7%. The dimensions of the samples and the experimentally determined Young's moduli, averaged over two tests, are given in Table 5.1. The tensile stress-strain responses are shown in Fig. 5.3(a) and Fig. 5.3(b). Because the fibers are enclosed by rubber layers, the load is initially carried by the inner rubber layer, resulting in a compression of this layer at the rings in the tensile direction. In Fig. 5.3(a) and(b) this is observed as an initial lower stress-strain rate.

The experiments discussed above are simulated with MARC. The same dimensions are used as given in Table 5.1 and the material (composite) structure of the fiber reinforced rubber material is implemented as discussed in chapter 4, section 4.2.2. The calculated Young's moduli are given in Table 5.1, whereas the stress-strain responses are also shown in Fig. 5.3(a) and (b).

Because the leaflets in the numerical model of the aortic valve prosthesis show large

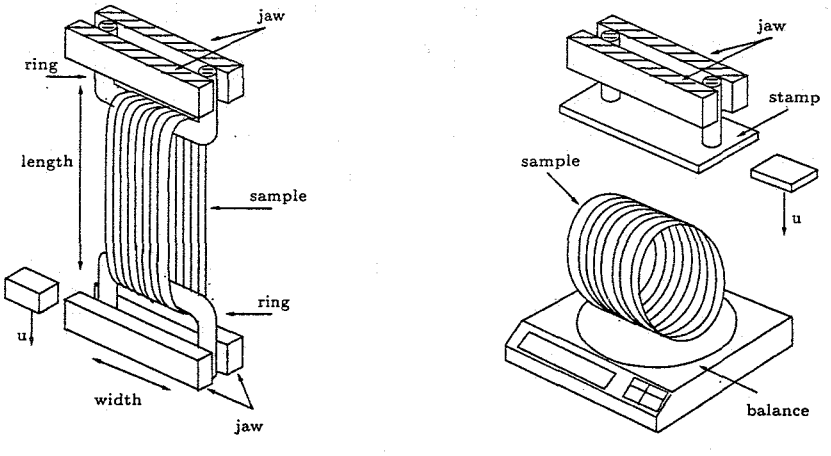

(a) tensile test (b) bending test

Figure 5.2: *Tensile and bending tests set-up for fiber reinforced tube shaped samples.*

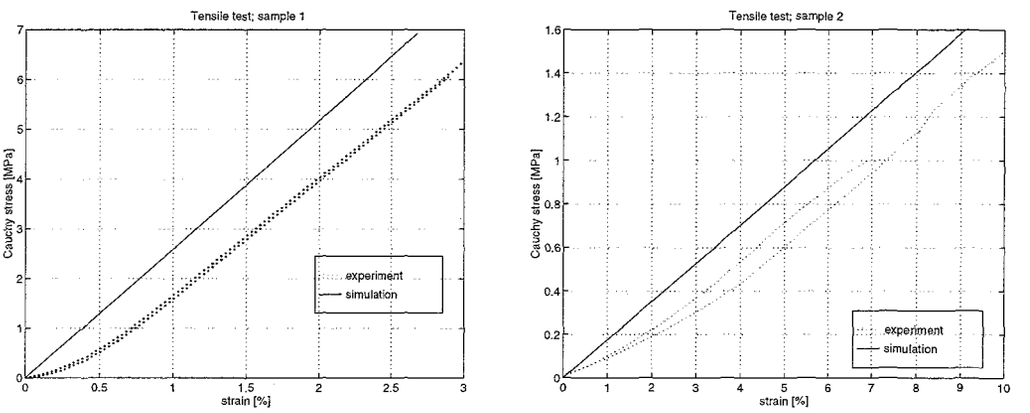

(a) sample 1 (b) sample 2

Figure 5.3: *Stress-strain responses of tensile tests on (a) sample 1 and (b) sample 2.*

bending deformations, a simple bending test is performed on a tube shaped sample with a unidirectional shaped reinforcement of 21 fibers (sample 3 Fig. 5.1(c)). Again, the 'Zwick' machine is used, together with a high accuracy balance on which the sample is laid down (Fig. 5.2(b)). As the upper stamp moves down with small displacement steps, the reaction force on the balance is measured in mN's. The dimensions of the sample as well as the reaction force-displacement ratio (F_r/u) between displacements of 3 mm and 8 mm (averaged over two tests) are given in Table 5.1. The bending reaction force-displacement response is shown in Fig. 5.4.

Again, this test is simulated using the same dimensions and material properties as the tested sample (Fig. 5.1(c)). The material structure is implemented as discussed in chapter 4, section 4.2.2. The calculated reaction force-displacement ratio is given in Table 5.1 and the reaction force-displacement response is also shown in Fig. 5.4.

From the results presented in Fig. 5.3 and Fig. 5.4 it is speculated that tensile and bending experiments on leaflet material structures can be simulated numerically using the material

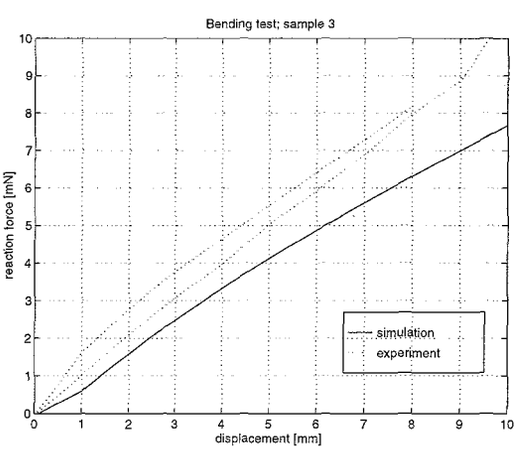

Figure 5.4: *Reaction force-displacement responses of bending tests on sample 3.*

	dimensions			**fibers**	***E*-mod.** (MPa)	
	length (mm)	width (mm)	thick. (μm)	#	exp.	num.
sample 1	34	17	330±10	17	244	258
sample 2	31	21	100±10	15	16	18
sample 3	22*	18	300±20	21	0.90**	0.78**

Table 5.1: *Dimensions and results of samples 1 and 2 under tensile load and sample 3 under bending load; * diameter of sample (mm), ** F_r/u ratio(mN/mm)*

modeling described in chapter 4, section 4.2.2. A slight difference between the Young's moduli and the F_r/u ratio can be caused by the linear elastic material modeling and the non-uniform thicknesses of the samples.

5.3 Numerical Solution Problems

The numerical model of the aortic valve prosthesis is solved using 'Path-Following' algorithms as described in chapter 4, section 4.3.4. However, numerical problems occur in some cases of fiber reinforcement when using the original values for the fiber modulus E_f (30 GPa; section 4.2.2) and the applied pressure load (12 kPa; section 4.2.3). In general, these problems arise from the solution procedure discussed in chapter 4, section 4.3.

The model of the valve prosthesis shows locally many bifurcation points, which separate different equilibrium paths that are either stable or unstable (section 4.3.3.). Stability analysis of the system determine the choice of the equilibrium path that is taken. If equilibrium states are nearly identical just beyond bifurcation points, a different equilibrium path can be taken which can lead to very different deformations. This problem is mainly caused by the imperfection of the model and its high degree of mobility, resulting in more (un)stable equilibrium conditions (section 4.3.3). At this time it is not possible to control the choice of the desired equilibrium path.

The use of quadratic constraint equations in 'Path-Following' algorithms has in general two advantages when compared to linear constraint equations. Mostly, convergence is reached in less iteration steps and, at bifurcation points, a solution is found within the critical area, which implies that the (unstable) equilibrium path in the 'snap-through' area is encountered. As for example 3, section 4.3.3, this means that at bifurcation point B the next solution is found on the BC portion of the curve instead of directly going to solution C (Fig. 4.10). However, when having two possible roots for the quadratic constraint equation the wrong solution can be taken at critical points, which mostly leads to a reversion along the same equilibrium path. With the use of subroutines the choice of root can be controlled and a normal deformation pattern can be obtained. In some cases no real roots can be found for the quadratic constraint equation. Using linear constraint equations is an alternative, however, numerical experiments showed that other problems, such as divergence, were then inevitable. Moreover, when not controlling the pressure load carefully at critical points, divergence systems were also the result.

As a solution to the numerical problems discussed above, two adjustments are introduced in the model that lead to convergent simulations for all fiber reinforcements analyzed in this report: the fiber modulus is set to 10% ($\hat{E}_f = 3$ GPa) of the longitudinal Young's modulus E_f; the applied pressure is 33% (4 kPa) of the maximum pressure difference measured over

the leaflets in the 'pulse duplicator' (section 3.5). A fiber modulus $\hat{E}_f = 3$ GPa is admissible, since it is still much higher than the matrix modulus E_m. Numerical experiments showed that this reduction has no consequences for the deforming character of the model and the stress distribution over the leaflet. However, some stresses that occur in the leaflet have a different value (section 5.4.4). Numerical experiments also showed that a pressure load of 4 kPa results in a full closed valve. Moreover, for some fiber reinforcements convergent simulations were obtained for a pressure load of 8 kPa showing very similar deformations when compared to a pressure load of 4 kPa. However, the difference in these deformations, although so little, result in significant stresses in the fibers of the model.

5.4 Results of Numerical Models

5.4.1 Introduction

This section discusses the results obtained from the numerical model described in chapter 4. First, the effect of upgrading the fiber modulus $\hat{E}_f$ from 30 MPa to 3 GPa on the stress distribution and the stress values in the leaflet is investigated. In subsection 5.4.3 the response of a non-reinforced model is, as far as possible, verified with results found in literature. The deformation of a fiber reinforced model is compared to the deformation of a prosthesis. Finally, the responses of four models with different fiber reinforcements are analyzed for the full closed valve and for the half closed valve (subsection 5.4.4).

In this section a distinction is made between the two outer rubber layers of the leaflet structure. The upper rubber layer, which is at the aorta side of the model, is referred to as the aortic rubber layer, whereas the lower rubber layer, which is at the ventricle side of the model is referred to as the ventricular rubber layer.

5.4.2 The Effect of Higher Fiber Moduli on Model Responses

A longitudinal fiber modulus $\hat{E}_f$ is used in the model which is 10% of the real fiber modulus E_f. The effect of this reduction on the model responses is investigated for an unidirectional, circumferential reinforced model with 10 fibers. The maximum principle stresses in the outer rubber layers of the leaflet composite structure as well as the maximum longitudinal and transversal stresses of the fiber reinforced layers are compared for fiber moduli of $\hat{E}_f = 30$ MPa, $\hat{E}_f = 300$ MPa and $\hat{E}_f = 3$ GPa, i.e. 0.1%, 1% and 10% of E_f respectively. For a closed configuration, at a pressure load of 4 kPa, and a half closed configuration effects on peak stress values are presented in Table 5.2.

For a half closed valve it is the configuration that is interesting rather than the associated pressure load for which this configuration is realized. However, similar half closed positions for the models with different $\hat{E}_f$ can not be obtained, since these configurations depend on the applied pressure load determined by the solution algorithm. It is not possible to control the applied load numerically in the snap-through area and therefore, half closed positions of the models are analyzed that are nearly equal. Corresponding figures of the stresses in the deformed models are found in Appendix C.

It is observed for the closed and half closed valve that an upgrade of the longitudinal fiber modulus in general does not affect the stress distribution over the leaflet (Appendix C). However, the maximum longitudinal stresses in the fiber reinforced layers increase, for the closed valve, with an averaged factor $\pm$ 2 and for the half closed valve with a factor

	closed				**$\frac{1}{2}$ closed**			
	MPSA	MPSV	MLS	MTS	MPSA	MPSV	MLS	MTS
$\hat{E}_f = 30$ MPa	1.26	0.455	1.19	0.623	0.166	0.138	0.131	0.155
$\hat{E}_f = 300$ MPa	0.952	0.432	3.46	0.520	0.165	0.139	0.171	0.165
$\hat{E}_f = 3$ GPa	0.733	0.394	6.07	0.553	0.174	0.135	0.236	0.174

Table 5.2: *The effect of $\hat{E}_f$ on maximum principle stresses in the aortic and ventricular rubber layer (MPSA and MPSV resp.) and on maximum longitudinal and transversal stresses in fiber layers (MLS and MTS resp.). The values are peak values in MPa.*

$\pm$ 1.3. The maximum principle stresses in the aortic rubber layer decrease with a factor $\pm$ 1.3 for the closed valve and are in the half closed situation nearly equal for a fiber modulus ten times as high. The model displacements, maximum transversal stresses in the fiber reinforced layers and the maximum principle stresses in the ventricular rubber layer are for both valve configurations less affected by a higher fiber modulus. It is expected that these conclusions apply to all fiber reinforced models discussed in this report. Therefore, values of above mentioned stresses should be interpreted carefully, when predicting stress values in the leaflets of the aortic valve prosthesis.

5.4.3 Verification of the Responses of Numerical Models

Verification of the stress responses in the leaflets with results found in literature is done for a closed non-reinforced model, since fiber-reinforced models have not been developed earlier. Maximum principle stresses in the outer layers of the leaflet structure are compared to results of [2], [5], [12].

A bi-leaflet bovine pericardium prosthesis with a non-linear elastic isotropic material behaviour and a closed stress-free configuration is modeled by Black [2]. For this model principle maximum stresses in the middle plane, upper plane and lower plane of shell elements were analyzed for a maximum pressure gradient over the valve of 11 kPa. There were areas with high stresses (425 kPa) found near the stent and the commissures. Chandran [5] modeled a polyurethane three-leaflet valve with a linear elastic isotropic material behaviour and a closed stress-free configuration. Again, shell elements were used and the maximum principle stresses were analyzed. Chandran found a maximum of 200 kPa in the coaptation area, close to the stent for a maximum pressure gradient of 10.6 kPa. Krucinski [12] also modeled a three-leaflet valve with a linear elastic isotropic material behaviour. This model is based on a pericardial valve, which had a half closed stress-free configuration. In the closed position there was a pick of the maximum principle stresses at the commissures (350 kPa) at a maximum pressure gradient over the valve of 11.9 kPa.

The models mentioned above all show the same area of maximum stresses. The numerical model discussed in this chapter shows similar areas of maximum stresses with a maximum value of 456 kPa in the ventricular rubber layer and a maximum value of 1.8 MPa in the aortic rubber layer (section 5.4.4) at a pressure load of 4 kPa. However, since the models of Black, Chandran and Krucinski all apply different pressures on the leaflets, which have different material properties, little information is obtained from a comparison of maximum stress values. Moreover, these models all show different stress-free configurations.

The response of a numerical model in terms of deformation is compared to the deformation of the aortic valve prosthesis in the 'pulse duplicator'. In an experiment a prosthesis with a

sinusoidal fiber reinforcement of 10 fibers is tested under a simulated physiological load. The deformation is recorded from the aortic side of the prosthesis with a high speed video-camera and the images are digitized. The response is shown in Fig. 5.5(a) for four stages in the loading cycle. The deformation of a numerical model with a corresponding stent geometry and fiber reinforcement is shown in Fig. 5.5(b). In this figure the distribution of the maximum principle stresses in the ventricular rubber layer of the leaflets is given.

During the experiments it is observed that the open configuration of the prosthesis is not cylindrical like the initial open stress-free position (Fig. 3.2(a)). This is mainly caused by the interaction of the leaflets with the fluid. The numerical model, however, does not take this interaction into account and therefore, the model shows its initial cylindrical configuration in the open position. In all other cases of Fig. 5.5 the deformed configurations are very similar. However, the heights of the leaflets of this prosthesis are larger than those in the model. Therefore, the leaflets of the prosthesis are coapting earlier than is observed for the leaflets in the numerical model. The space between two adjacent leaflets in the coaptation area of the numerical model in the closed configuration is a result of the used contact algorithm in MARC and is assumed to have no consequences for model responses. The influence of the sinusoidal fiber reinforcement on the stress distribution in the closed configuration of the model can easily be recognized. An analysis of stress distribution and values is done in the next subsections.

5.4.4 The Responses of Fiber Reinforced Models

Four fiber reinforced models are investigated for their response on a pressure load applied at the leaflets. Two models with an unidirectional, circumferential fiber reinforcement of 10 and 20 fibers are analyzed (uni-10 and uni-20 resp.), as well as two models with a sinusoidal fiber reinforcement of 10 and 20 fibers (sin-10 and sin-20 resp.) (Appendix A). The deformations, resulting from the applied pressure load, are nearly similar for all analyzed models.

It is suggested that failure of fiber reinforced prostheses is mainly caused by:

- longitudinal debonding of the fiber from the matrix ('pull-out')
- transversal debonding of the fiber from the matrix
- tearing and perforating of the rubber matrix material

These failure mechanisms are the result of undesired high stresses in critical areas of the leaflets and an inhomogeneous stress distribution in the leaflets. Therefore, the model responses are analyzed for maximum transversal and longitudinal stresses in the fiber layers (referred to as MTS and MLS resp.) and for maximum principle stresses in the outer rubber layers (referred to as MPSA for the aortic rubber layer and MPSV for the ventricular rubber layer). This is done for a closed configuration at a maximum pressure of 4 kPa and for a half closed configuration. Moreover, the results are compared to the MPSA and MPSV of a non-reinforced model.

Maximum stress values in peak areas are given for $1/6^{th}$ of the total valve as shown in Fig. 5.6. The actual peak areas for the analyzed stresses of the different models in the closed configuration are given in Fig. 5.7. Each area is identified with a letter and the corresponding stress values are shown in Table 5.3. The same is done for the half closed configuration (Fig. 5.8 and Table 5.4). In the remaining areas lower stresses occur that are expected to have a

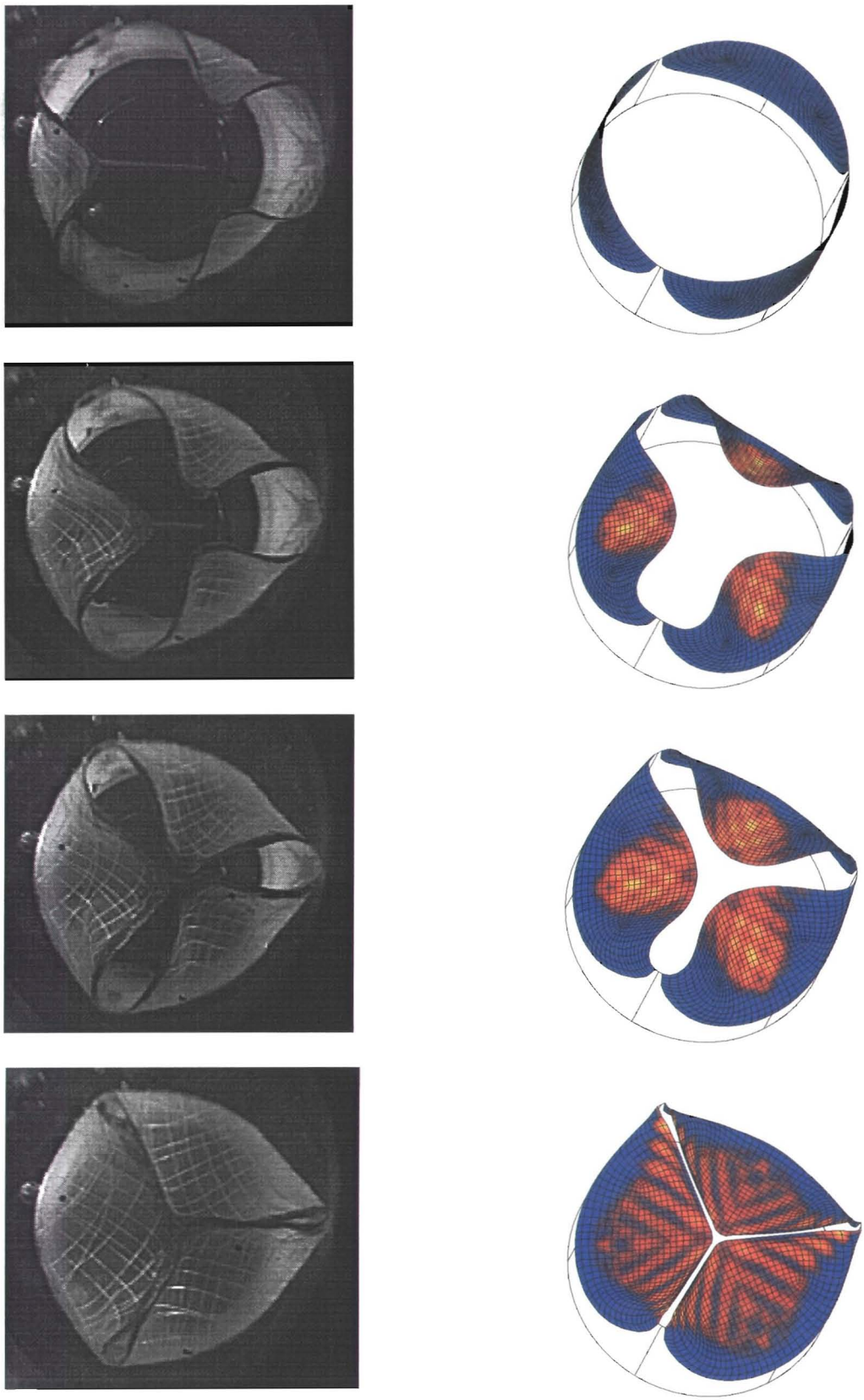

Figure 5.5: *Left: deformed configurations of a prosthesis under simulated physiological load; Right: deformed configurations of a corresponding numerical model.*

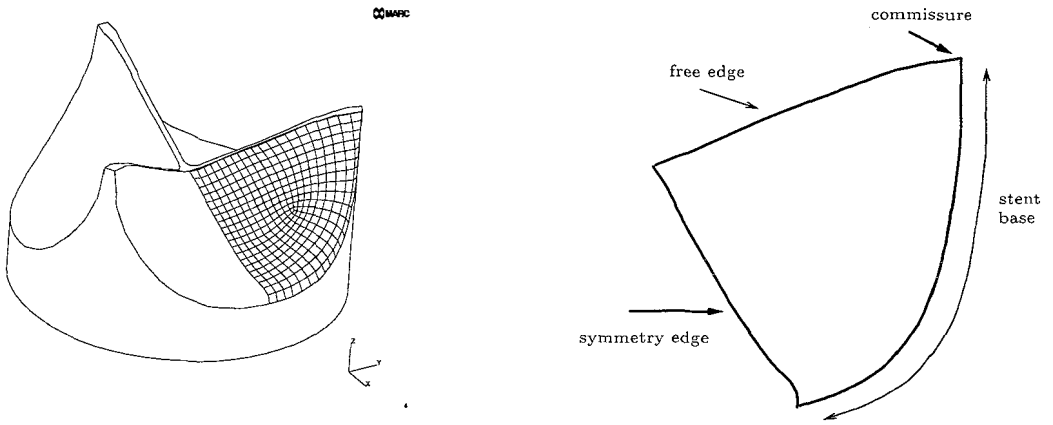

Figure 5.6: *(left) Closed valve with a mesh covering* $1/6^{th}$ *of the surface; (right) outline of the mesh used to define high stress areas.*

minor contribution to the failure behaviour of fiber reinforced prostheses. A full survey of the stress distributions over the leaflet is given in Appendix C.

From the stress values of Table 5.3 it is observed that for all fiber reinforced models lower peak values exist in the outer rubber layers compared to the non-reinforced model. Stresses in these layers are partly taken over by the fibers in the reinforced layers. The models uni-10 and uni-20 show a significant reduction of ±60% for the MPSA at the commissure (area A) in the aortic rubber layer. This reduction is less severe for peak area B near the stent base at the middle of the leaflet (±32%). For the models sin-10 and sin-20 stresses in these areas are reduced with ±30% and ±22% respectively.

In the ventricular rubber layer peak stresses (MPSV) appear near the commissure along the free edge (area C). These stresses are reduced from MPSV = 0.456 MPa with ±14% and ±38% for uni-10 and uni-20. For the models sin-10 and sin-20 this reduction is ±27% and ±46% respectively. So, the effect of doubling of the number of fibers in the leaflet is more significant for this layer than it is for the aortic rubber layer. However fiber reinforcements in general seem to affect stresses in the aortic rubber layer more seriously. An additional stress area arises for sin-10 (area D), which is also shown in Fig. 5.5. From this figure it is clear how the stress distribution is affected by the fiber reinforcement. The sinusoidal fiber

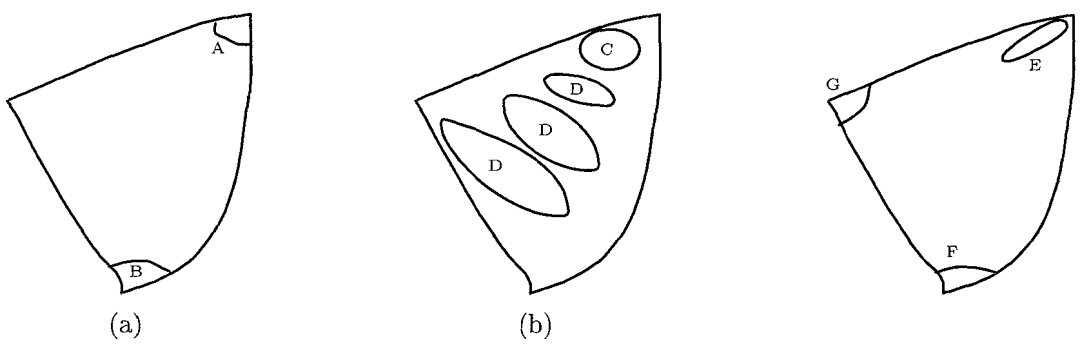

Figure 5.7: *Peak stress areas of the closed leaflet; (a) aortic rubber layer; (b) ventricular rubber layer; (c) reinforced layers. See text for explanation.*

closed	MPSA		MPSV		MLS			MTS	
config.	A	B	C	D	E	F	G	E	F
non-reinf.	1.81	0.812	0.456	-	-	-	-	-	-
uni-10	0.733	0.553	0.394	-	6.07	-	-	0.471	0.553
uni-20	0.697	0.539	0.283	-	7.31	-	-	0.601	0.560
sin-10	1.28	0.592	0.333	0.278	15.1	3.11	-	0.996	0.552
sin-20	1.30	0.653	0.247	-	17.3	7.15	3.33	0.934	0.582

Table 5.3: *Peak stress values of the closed models associated with the peak stress areas. Stress values are given in MPa. See text for explanation.*

reinforcement can actually be recognized, as it has taken over maximum principle stresses in this rubber layer.

Maximum longitudinal stresses (MLS) appear in the reinforced layers at the commissure and along the free edge near the commissure (area E). High MLS of ±16 MPa occur for the sinusoidal reinforcements, which are at least twice as high than the MLS of the unidirectional, circumferential reinforcements. Moreover, a peak area is centered at the middle of the leaflet near the stent base (area F) for these sinusoidal reinforced models with a maximum stress of 7.15 MPa for sin-20. An additional high stress area is found for sin-20 at the free edge in the middle of the leaflet (area G) with a MLS of 3.33 MPa. Maximum transversal stresses (MTS) in the reinforced layers occur in areas E and F. In area E a maximum value of 0.996 MPa is found for sin-10. Stresses in area F are on the other hand very similar for all discussed reinforced models (±0.561 MPa).

Peak areas for the half closed valve are given in Fig. 5.8 (Notice the different shape of the leaflet). The corresponding stress values are given in Table 5.4. Similar half closed positions can not be obtained as mentioned in section 5.4.3, however, configurations are analyzed that are almost equal.

From the stress values given in Table 5.4 it is observed that all fiber reinforcements result in lower peak stresses for the aortic rubber layer compared to the non-reinforced model. For peak values of the MPSA along the base stent (area A) and at the base stent in the middle of the leaflet (area B) a maximum reduction is found of ±41% and ±55% respectively for uni-20. High stress areas in the ventricular rubber layer appear in the center of the leaflet towards the free edge (area C). The MPSV in this layer is maximum reduced with ±32% for sin-20 and is hardly affected for uni-10 and sin-10.

Maximum longitudinal stresses (MLS) appear in the reinforced layers along the free edge (area D). High MLS occur for sin-20, which is 3 times as high than the MLS of uni-10. An additional peak area is found at the stent base in the middle of the leaflet for sinusoidal reinforced models with a maximum stress of 1.52 MPa for sin-20. Maximum transversal stresses (MTS) occur in areas D and E for all reinforced models. The MTS values in area D are nearly equal for all reinforced models, whereas in area E a maximum value of 0.186 MPa is found for sin-20.

In Appendix C figures are shown with the stress distributions of the different models. From these figures it appears that in the half closed configuration stress distributions of maximum principle stresses in the outer rubber layers are almost independent of fiber reinforcements. The stress distributions of maximum longitudinal stresses in the reinforced layers and maximum principle stresses in the ventricular rubber layer become in the half closed

1/2 closed config.	MPSA A	B	MPSV C	MLS D	E	MTS D	E
non-reinf.	0.189	0.251	0.136	-	-	-	-
uni-10	0.148	0.174	0.135	0.236	-	0.109	0.174
uni-20	0.111	0.114	0.114	0.657	-	0.108	0.115
sin-10	0.144	0.160	0.143	0.527	0.489	0.090	0.160
sin-20	0.132	0.186	0.092	0.712	1.52	0.113	0.186

Table 5.4: *Peak stress values of the half closed models associated with the peak stress areas. Stress values are given in MPa. See text for explanation.*

and closed situation very inhomogeneous for sin-10 compared to the other reinforced models. However, increasing the number of fibers results in more homogeneous distributions for these stresses. The fiber reinforcement of sin-20 results in the most homogeneous stress distribution for the maximum transversal stresses in the reinforced layers and the maximum principle stresses in the outer rubber layers in both the closed and half closed situation. The maximum longitudinal stress distribution is on the other hand very irregular in the closed situation.

From the results discussed above, no reinforced model discussed in this report is categorized as the best with respect to the failure mechanisms of the fiber reinforced prostheses. For all reinforced models stresses are reduced in the weaker parts of the leaflet, i.e. the outer rubber layers. When analyzing stress values in peak stress areas it can be concluded that uni-20 has the least stress baring outer rubber layers in both the closed and half closed configuration. On the other hand, uni-10 shows the lowest maximum longitudinal and transversal stresses in the fiber reinforced layers. Model sin-20 shows a very significant reduction of peak stress values in the ventricular rubber layer and has, except for maximum longitudinal stresses, the most homogeneous stress distribution compared to the other models.

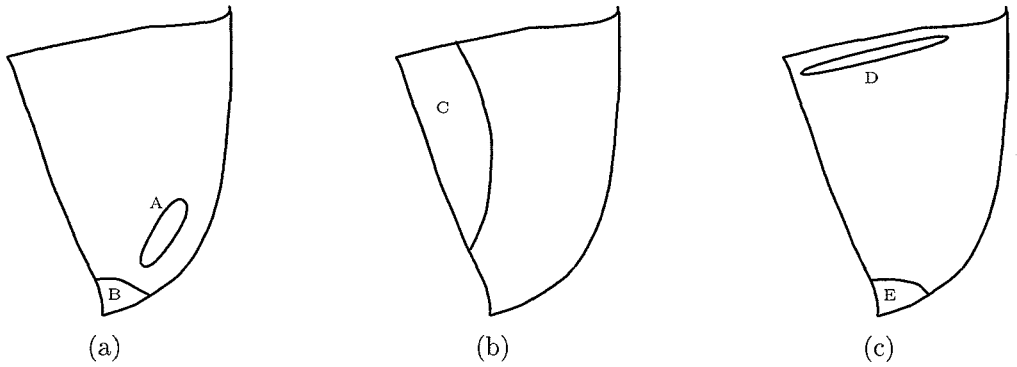

Figure 5.8: *Peak stress areas of the half closed leaflet; (a) aortic rubber layer; (b) ventricular rubber layer; (c) reinforced layers. See text for explanation.*

Chapter 6

General Conclusions and Recommendations

6.1 Introduction

In this chapter general conclusions and recommendations are presented referring to the numerical model of the three-leaflet aortic valve prosthesis. The conclusions as well as the recommendations relate to modeling aspects of the valve prosthesis, described in chapter 4, and the responses of numerical models, discussed in chapter 5. Moreover, recommendations are presented for future research on the mechanical behaviour of heart valve prostheses.

6.2 Conclusions

- Versatile, cylindrical shaped, fiber reinforcements can be designed for both experimental and numerical purposes.
- The implementation of reinforced leaflet material structures, as described in this report, is allowed to simulate tensile and bending behaviour.
- Convergent problems occur for numerical models in some cases of fiber reinforcement.
- Lower longitudinal fiber moduli and pressure loads result in convergent simulations for all fiber reinforcements discussed in this report. Therefore, models are analyzed with these lower values.
- Lower longitudinal fiber moduli in general do not affect the stress distributions over the valve. However, stress values should be interpreted carefully for prediction of stresses in corresponding prostheses.
- High stress areas occur that correspond with high stress areas found in the literature.
- Similar deformations are observed for a numerical model when compared to a corresponding prosthesis.
- Different fiber reinforcements do not affect deformation patterns.

- Maximum principle stresses in the outer rubber layers of the leaflet structure are, for the analyzed models in this report, reduced with maximum 60% with respect to non-reinforced models.
- No particular fiber reinforcement, analyzed in this report, is categorized as most appropriate for the use in valve prostheses.

6.3 Recommendations

- Other solution strategies are desired for numerical simulations of the three-leaflet aortic valve prosthesis with original values for longitudinal fiber moduli and pressure loads.
- The contact algorithm of the numerical model should be changed in order to get full closure of the valve.
- Fluid interactions should be modeled, as well as a physiological pressure load in order to get a more realistic model.
- More different fiber reinforcements should be analyzed, e.g. a more natural reinforcement, in order to get an optimum design referring to the failure of valve prostheses.
- A more detailed verification of numerical results should be done.
- In future research affection on model responses should be analyzed for:
  - variable leaflet thicknesses.
  - variable leaflet heights
  - variable stent geometries.
  - flexible stents.

References

[1] Bernacca, G., Mackay, T., and Wilkinson, R. Calcification and fatigue failure in a polyurethane heart valve. *Biomaterials 1995*, 16:279–284, 1995.

[2] Black, M.M., Howard, I.C., Huang, X., and Patterson, E.A. A three-dimensional analysis of a bioprosthetic heart valve. *J. Biomechanics*, 24:793–801, 1991.

[3] Brewer, R.J., Mentzer, R.M., Deck, J.D., and Nolan, S.P. An in vivo study of the dimensional changes of the aortic valve leaflets during the cardiac cycle. *J. Cardiovasc. Surg.*, 74:645–653, 1977.

[4] Cacciola, G. Development and testing of a synthetic fibre reinforced three-leaflet heart valve. Technical report, Eindhoven University of Technology, The Netherlands, 1996.

[5] Chandran, K.B., Kim, H.H., and Han, G. Stress distribution on the cusps of a polyurethane trileaflet heart valve prosthesis in the closed position. *J. Biomechanics*, 24:385–395, 1991.

[6] Chrisfield, M.A. *Variable step-lengths for non-linear structural analysis.* PhD thesis, Transport and road research laboratory report 1049, Berkshire, 1982.

[7] CTD, Magazijn technische materialen, Nr. 13.2.4. *TUE intern normblad.*

[8] Gross, G. and Kugel, M.A. Topographic anatomy and histology of the valves in the human heart . *Am. J. Pathol.*, 43:184–191, 1971.

[9] Halpin, J.C. *Primer on composite materials analysis.* Wright-Patterson AFB, Ohio, 1992.

[10] Konter, A.W.A. *Analysis of composite materials.* MARC Analysis Research Corporation, 1992.

[11] Kouhia, R. and Mikkola, M. Tracing the equilibrium path beyond simple critical points. *Int. J. for Num. Methods in Engineering*, 28:2923–2941, 1989.

[12] Krucinski, S., Vesely, I., Dokainish, M.A., and Campbell, G. Numerical simulation of leaflet flexure in bioprosthetic valves mounted on rigid and expansile stents. *J. Biomechanics*, 26:929–943, 1993.

[13] Lemstra, A.W. Heart valves: facts and visions. Technical Report WFW 96.126, Eindhoven University of Technology, The Netherlands, 1996.

[14] MARC Analysis Research Corporation, Zoetermeer, Zuid-Holland. *MARC Program Input vol. A5-4*, 1996.

[15] MARC Analysis Research Corporation, Zoetermeer, Zuid-Holland. *MARC Program Input vol. A5-42*, 1996.

[16] MARC Analysis Research Corporation, Zoetermeer, Zuid-Holland. *MARC User Subroutines and Special Routines vol. D1-219*, 1996.

[17] Mast, F., Hoschtitzky, J., and B. andHuysmans, H.A. In vitro biocompatibility of EPM- and EPDM-rubers. *in press in J. of Material Science, Material in Medicine.*

[18] Peijs, A.A.J.M. *High-performance polyethylene fibers in structural composites? Promises, Reality and applications in hybrid composites.* PhD thesis, Eindhoven University of Technology, 1993.

[19] Rousseau, E.P.M. *Mechanical specifications for a closed leaflet valve prosthesis.* PhD thesis, Eindhoven University of Technology, 1985.

[20] Sauren, A.A. and Kuypers, W. Aortic valve histology and its relation with mechanics. *J. Biomechanics*, 13:97–104, 1980.

[21] Sauren, A.A.H.J. *The mechanical behaviour of the aortic valve.* PhD thesis, Eindhoven University of Technology, 1981.

[22] Simitses, G.J. *An introduction to the elastic stability of structures.* Prentice-Hall Inc., Englewood Cliffs, New Jersey, 1976.

[23] Swartjes, F.H.M. Making a heart valve prototype of EPDM rubber reinforced with PE or lycra fibers. Technical Report WFW 95.150, Eindhoven University of Technology, The Netherlands, 1995.

[24] Thompson, J.M.T. and Hunt, G.W. *A general theory of elastic instability.* John Wiley and Sons Ltd., 1973.

[25] Thompson, J.M.T. and Hunt, G.W. *Elastic instability phenomena.* John Wiley and Sons Ltd., 1984.

[26] Wheatly, D.J., Fisher, J., Reece, I.J., and Breeze, P. Primary tissue failure in pericardial heart valves. *J. Thorac. Cardiovasc. Surg.*, 94:367–374, 1987.

Appendix A

Computer Designed Fiber Layouts to Reinforce Tube Shaped Structures

In this appendix computer designed fiber layouts are presented that are used to reinforce tube shaped structures. Computer programs are developed in MatLab 4.2 for the generation and implementation of fiber layouts, which can be used for both experimental and numerical purposes. The fiber layouts that are used in the reinforced models of the aortic valve prostheses, described in this report, are also shown. The unidirectional, circumferential fiber reinforcements are shown in Fig. A.1 for 10 (uni-10) and 20 (uni-20) fibers respectively. The sinusoidal reinforcements of 10 (sin-10) and 20 (sin-20) fiber are shown in Fig. A.2. The sinusoidal reinforcements have a parabolic variable height, since the leaflets in the protheses show a semi lunar shape. In the left picture of Fig A.3 a fiber layout is shown with linear variable heights. For the use of flexible stents in valve prostheses fiber layouts can be designed to reinforce the stent structure. A typical reinforcement for flexible stents is given in the right picture of Fig. A.3.

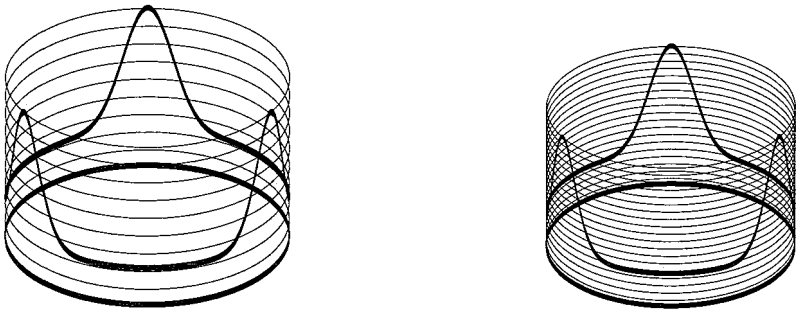

(a) (b)

Figure A.1: *Unidirectional, circumferential fiber reinforcements of 10 (uni-10) and 20 (uni-20) fibers.*

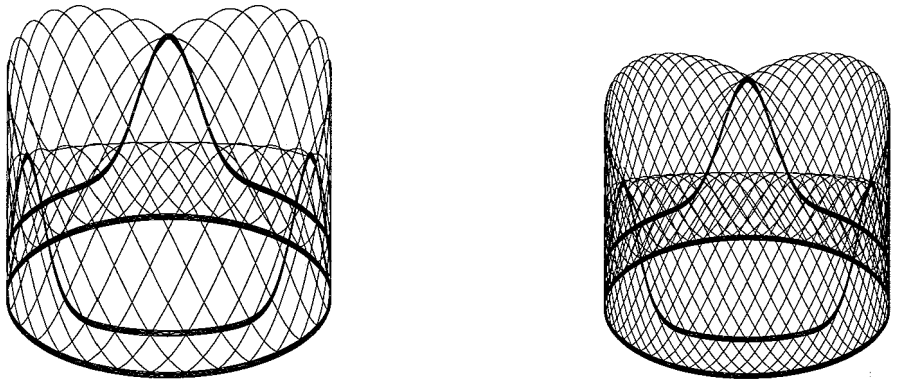

(a) (b)

Figure A.2: *Sinusoidal fiber reinforcements of 10 (sin-10) and 20 (sin-20) fibers.*

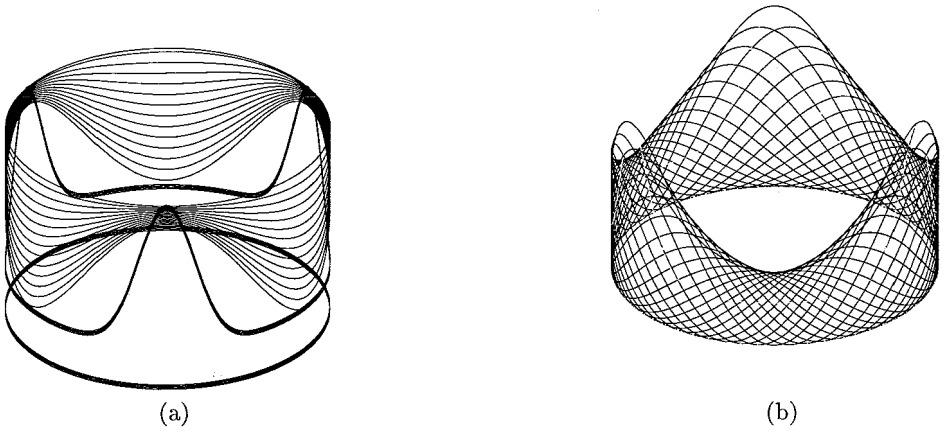

(a) (b)

Figure A.3: *A linear variable sinusoidal fiber reinforcement (Left) and a typical fiber reinforcement used for flexible stents (Right).*

Appendix B

Coordinate Systems in MARC

B.1 Three-Dimensional Bilinear Thick-Shell Element

Consider a three-dimensional thick-shell element in a Carthesian coordinate system, also *Global Coordinate System* (GCS). The element is defined geometrically by the (x, y, z) coordinates of the four corner nodes. Due to bilinear interpolation the surface will form a hyperbolic paraboloid which is allowed to degenerate to a plane. The element thickness is specified in the "GEOMETRY" option. The stress and strain output is given in local orthogonal surface coordinate directions, $\{\vec{V}_1, \vec{V}_2, \vec{V}_3\}$, or *Surface Coordinate System* (SCS), which for the centroid of the element are defined in the following way (see Fig. A.1):

At the centroid the vectors $\{\vec{t}_1, \vec{t}_2\}$ tangent to the curves with constant isoparametric coor-

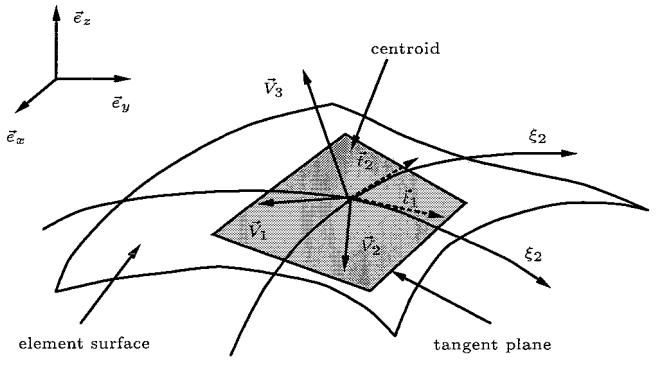

Figure B.1: *Surface Coordinate System of a three-dimensional thick-shell element.*

dinates (ξ_1 and ξ_2) are normalized.

$$\vec{t}_1 = \frac{\delta x}{\delta \xi_1} / |\frac{\delta x}{\delta \xi_1}| \quad ; \quad \vec{t}_2 = \frac{\delta x}{\delta \xi_2} / |\frac{\delta x}{\delta \xi_2}| \tag{B.1}$$

From these normalized vectors, a new basis is being defined as of which the local orthogonal directions $\{\vec{V}_1, \vec{V}_2, \vec{V}_3\}$ are then obtained (MARC manual B3-75)

$$\hat{\vec{s}}_1 = \vec{t}_1 + \vec{t}_2 \quad \rightarrow \quad \vec{s}_1 = \hat{\vec{s}}_1 / \|\hat{\vec{s}}_1\| \tag{B.2}$$

$$\hat{\vec{s}}_2 = \vec{t}_1 - \vec{t}_2 \quad \rightarrow \quad \vec{s}_2 = \hat{\vec{s}}_2 / \|\hat{\vec{s}}_2\| \tag{B.3}$$

For the local orthogonal directions follows

$$\vec{V}_1 = \vec{s}_1 + \vec{s}_2 \quad ; \quad \vec{V}_2 = \vec{s}_1 - \vec{s}_2 \quad ; \quad \vec{V}_3 = \vec{V}_1 * \vec{V}_2 \tag{B.4}$$

The orthogonal directions $\vec{V}_1$ and $\vec{V}_2$ are situated in the tangent plane at the centroid of the element, whereas $\vec{V}_3$ is perpendicular directed to this plane. With user-subroutines it is possible to define the *Surface Coordinate System* in each integration point of the element, however, within MARC normally this is done in the middle of the element ($\xi_1 = \xi_2 = 0$). As the stress and strain output is given in the *Surface Coordinate System*, interpretation of these variables is difficult, since the *Surface Coordinate System* can be different for each element. In behalf of this interpretation of the calculated stresses and strains, a suitable *Material Coordinate System* (MCS) can be defined with the "ORIENTATION" option within MARC.

B.2 The *Material Coordinate System* in MARC

The default MARC *Material Coordinate System* is equal to the *Surface Coordinate System.* For the use of a more appropriate *Material Coordinate System* , new orthogonal coordinate directions $\{\vec{m}_1, \vec{m}_2, \vec{m}_3\}$ are defined with the "ORIENTATION" option. The directions of the *Material Coordinate System* can for each element be defined locally or globally, or with the user subroutine ORIENT for each integration point of the element (MARC manual A6-5, C3-266 and Volume D). Basically, a reference plane or edge is taken with respect to which the orthogonal coordinate directions $\{\vec{m}_1, \vec{m}_2, \vec{m}_3\}$ are defined. For example, this can be the zx-plane of the *Global Coordinate System*, locally an element edge or an user defined plane, as shown in Fig. A.2. In each case the third vector of the *Material Coordinate System* is:

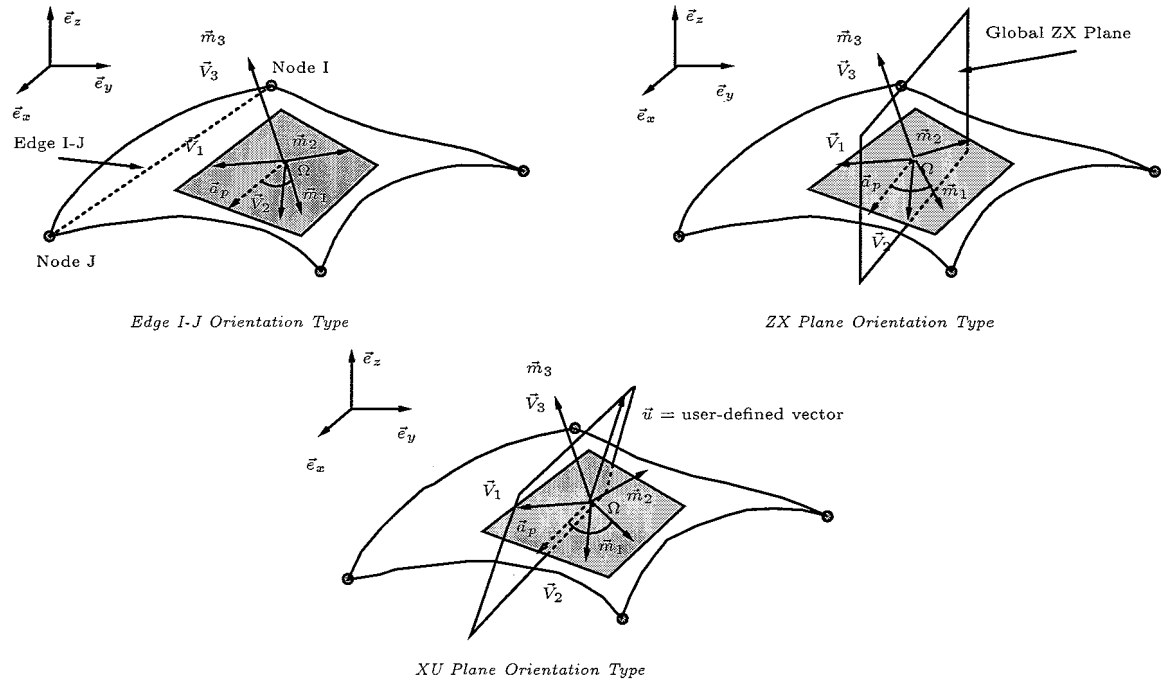

Figure B.2: *Material Coordinate Systems defined by different Orientation types.*

$\vec{m}_3 = \vec{V}_3$. The two other vectors ($\vec{m}_1$ and $\vec{m}_2$) are situated in the tangent plane at the centroid of the element. An unit vector $\vec{a}$ is defined, which is tangentially directed to the reference plane or edge, chosen in the "ORIENTATION" option. This vector is then projected on the tangent plane at the centroid of the element: $\vec{a} \rightarrow \vec{a}_p$. The first vector of the *Material Coordinate System* $\vec{m}_1$ is taken with respect to $\vec{a}_p$ after a rotation along $\vec{m}_3$ with an orientation angle Ω, specified by the user. The second vector of the *Material Coordinate System* $\vec{m}_2$ is equal to $\vec{m}_2 = \vec{m}_3 * \vec{m}_1$.

The output of stresses and strains can be given with respect to this coordinate system. In some situations stress and strain output is desired in a preferred direction with respect to this coordinate system. A *Preferred Coordinate System* can be defined to get stress and strain output in this preferred direction.

B.3 The *Preferred Coordinate System* in MARC

When modeling material with different principal material directions for each element, it is desired to orient the *Material Coordinate System* in these principal material directions. The directions of the material are default taken with respect to the *Surface Coordinate System.* Using the *Material Coordinate System* defined with the "ORIENTATION" option these direction of the material are taken with respect to this coordinate system. From this system a *Preferred Coordinate System* can be defined with orthogonal coordinate directions $\{\vec{p}_1, \vec{p}_2, \vec{p}_3\}$ of which $\vec{p}_3 = \vec{m}_3 = \vec{V}_3$ and $\vec{p}_1$ is obtained from a rotation of the vector $\vec{m}_1$ along $\vec{m}_3$ with angle α, specified by the user, which can be different for each element. (Fig. A.3). This angle α is also the ply angle of a lamina when using the "COMPOSITE" option (MARC manual C3-267). The vector $\vec{p}_2$ is defined with $\vec{p}_2 = \vec{p}_3 * \vec{p}_1$. The transformation of the *Surface Coor-*

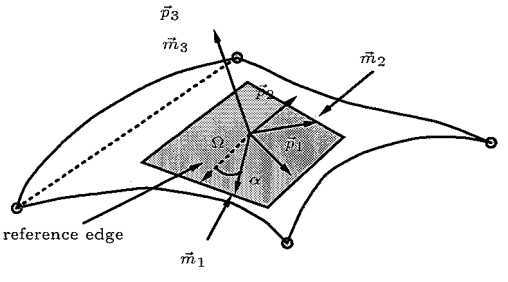

Figure B.3: *Preferred Coordinate Systems defined with regard to a reference edge.*

dinate System to a user defined *Preferred Coordinate System* from the *Material Coordinate System* results in an output of stresses and strains in a user defined preferred direction, which is equal to the chosen reference plane or edge in the "ORIENTATION" option after a rotation over a preferred angle $(\Omega + \alpha)$.

Appendix C

Stress Distributions in (Non-)Reinforced Aortic Valve Models

In this appendix stress distributions are shown in the leaflet of the numerical model of the three-leaflet aortic valve prosthesis. Closed and half closed configurations are presented for the fiber reinforced models discussed in this report. Moreover, the stress distribution of a non-reinforced model is given Fig. C.1. For all models maximum principle stresses in the outer rubber layers of the leaflet material structures are considered. Distributions of maximum longitudinal and transversal stresses in the fiber reinforced layers are also given for the reinforced models. In Fig. C.2 and C.3 the closed and half closed configurations are shown for a model with 10 fibers with a unidirectional, circumferential orientation (Appendix A). The fibers in this model have a longitudinal modulus of 30 MPa. Similar models with longitudinal fiber moduli of 300 MPa and 3 GPa are shown in Fig. C.4 to C.7. A model with 20 fibers in a unidirectional, cicumferential orientation is presented in Fig. C.8 and C.9. The stress distributions of sinusoidal fiber reinforced models with 10 and 20 fibers are shown in Fig. C.10 and C.11 and in Fig. C.12 and C.13 respectively.

This Appendix only considers the stress distributions and therefore, real stress values are not given. Significant stress values are presented in chapter 5 of this report. The scales in the figures are for all cases set to equal ranges in order to compare distributions between the different models. However, for stresses in the reinforced layers scales are not equally set, since peak stresses in these layers can be very different between models.

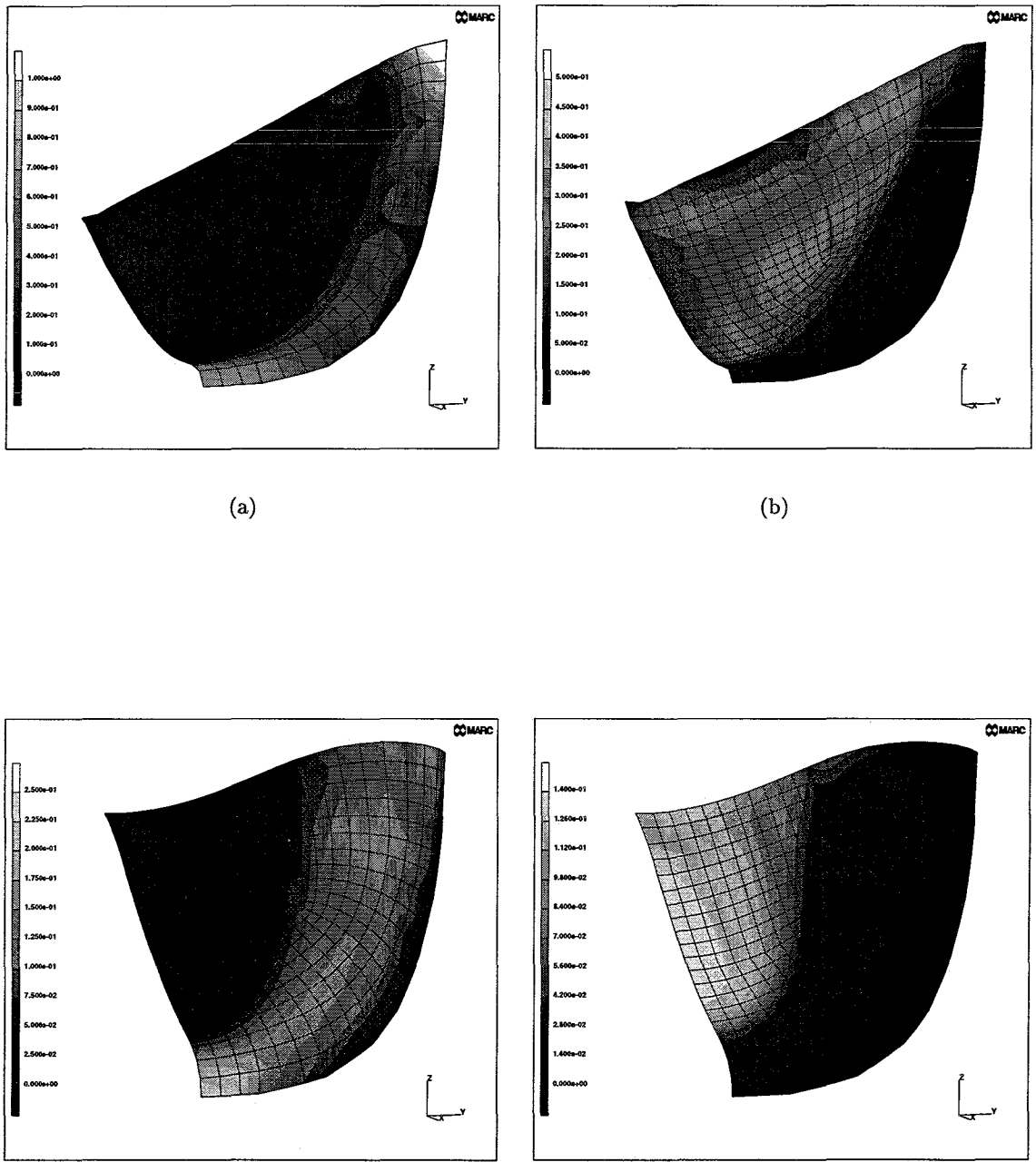

Figure C.1: *Stress distributions of a non-reinforced model. Maximum principle stresses in the aortic rubber layer (a and c) and the ventricular rubber layer (b and d) in closed and half closed configurations respectively.*

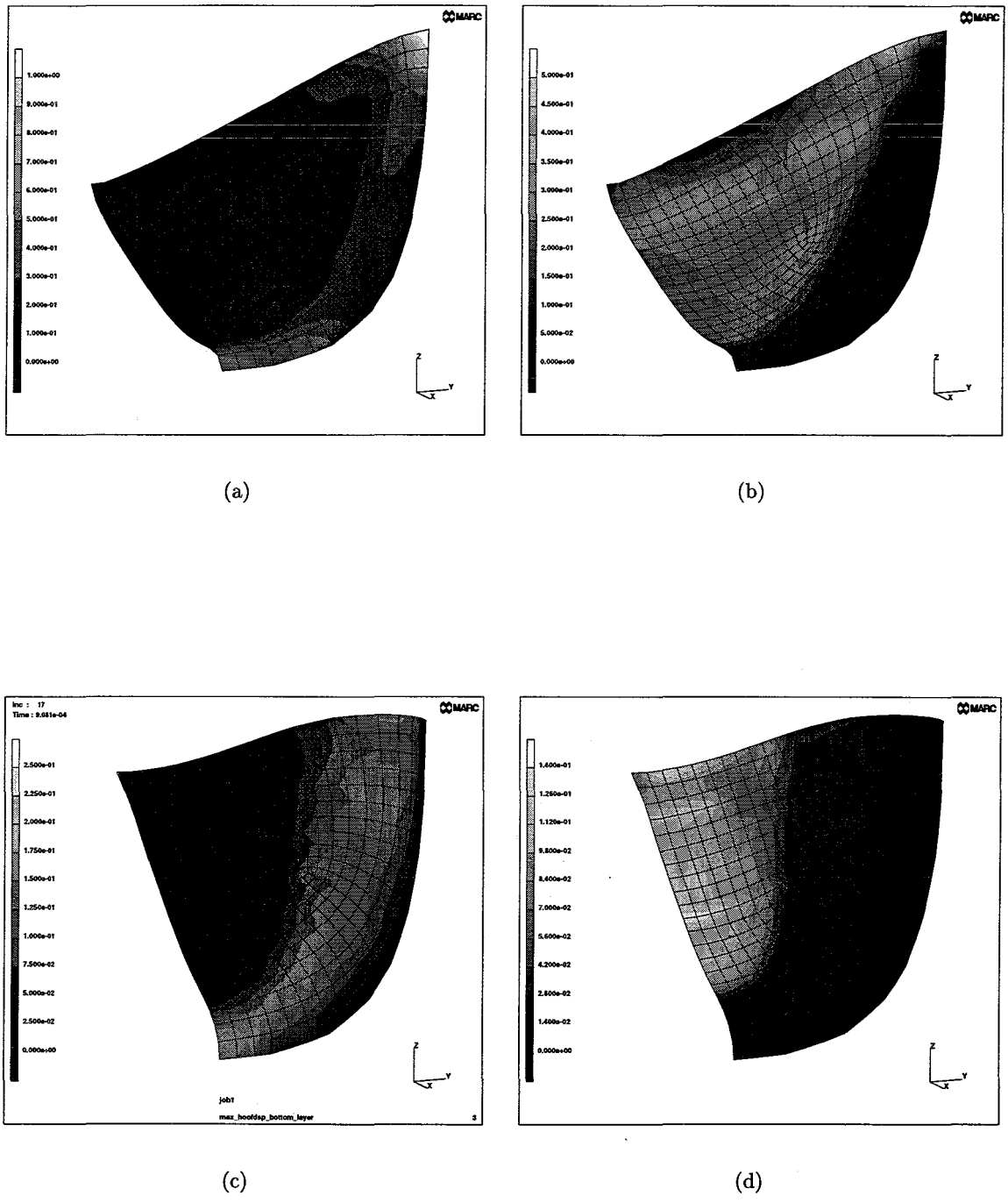

(a) (b)

(c) (d)

Figure C.2: *Stress distributions of a unidirectional, circumferential reinforced model with 10 fibers and a fiber modulus of 30MPa. Maximum principle stresses in the aortic rubber layer (a and c) and the ventricular rubber layer (b and d) in closed and half closed configurations respectively.*

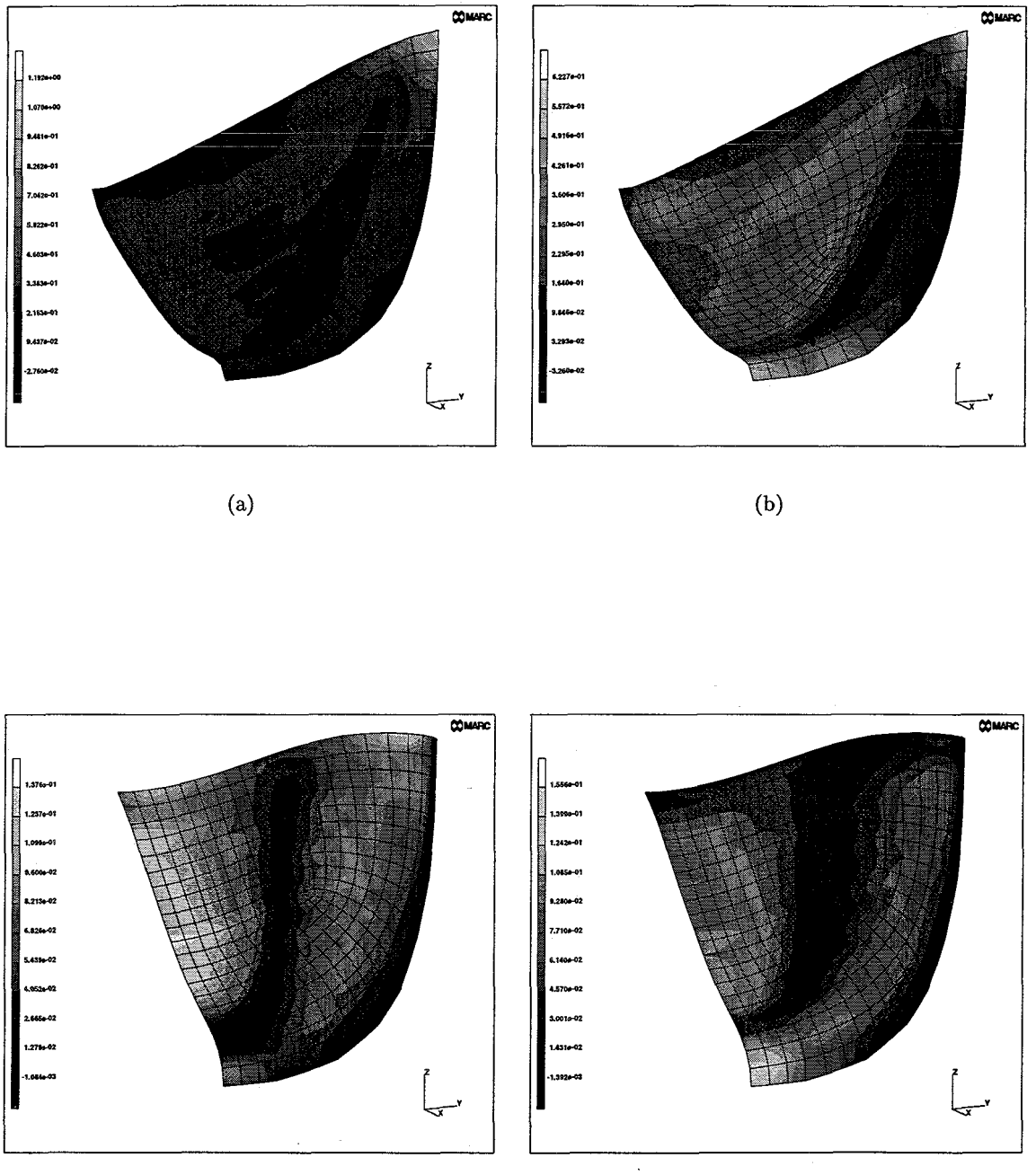

Figure C.3: *Stress distributions of a unidirectional, circumferential reinforced model with 10 fibers and a fiber modulus of 30 MPa. Maximum longitudinal stresses (a and c) and maximum transversal stresses (b and d) in closed and half closed configurations respectively.*

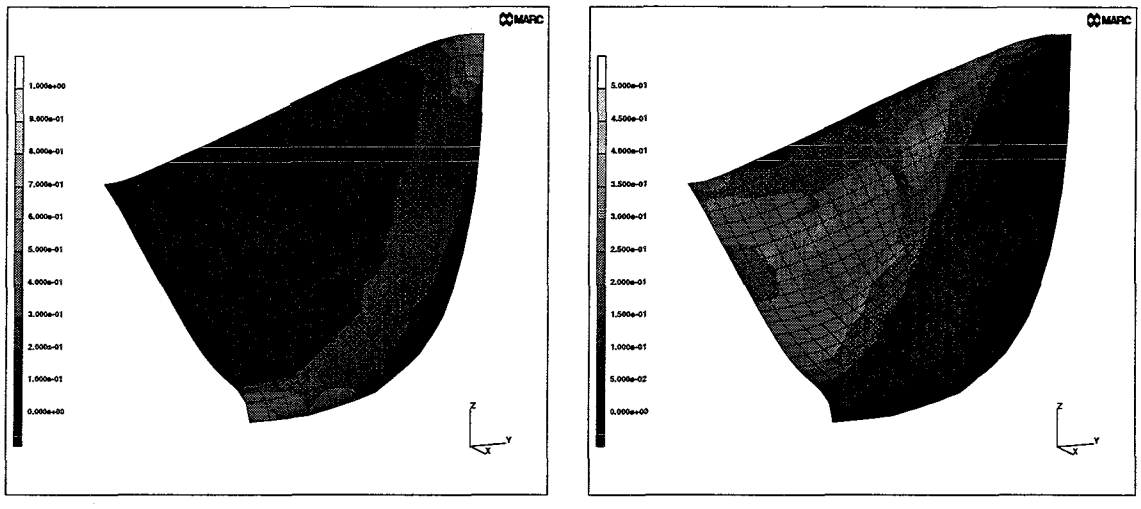

(a) (b)

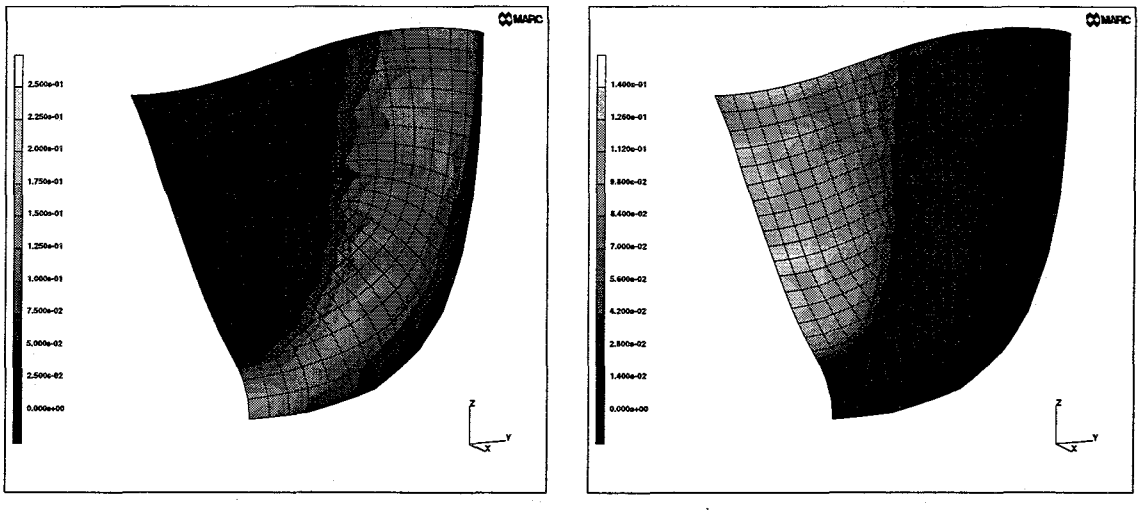

(c) (d)

Figure C.4: *Stress distributions of a unidirectional, circumferential reinforced model with 10 fibers and a fiber modulus of 300 MPa. Maximum principle stresses in the aortic rubber layer (a and c) and the ventricular rubber layer (b and d) in closed and half closed configurations respectively.*

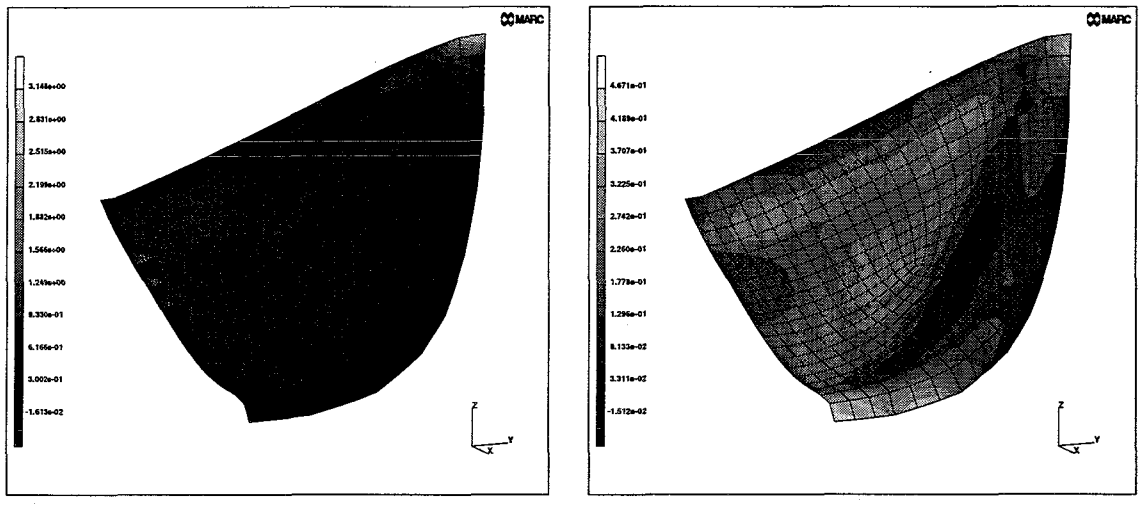

(a) (b)

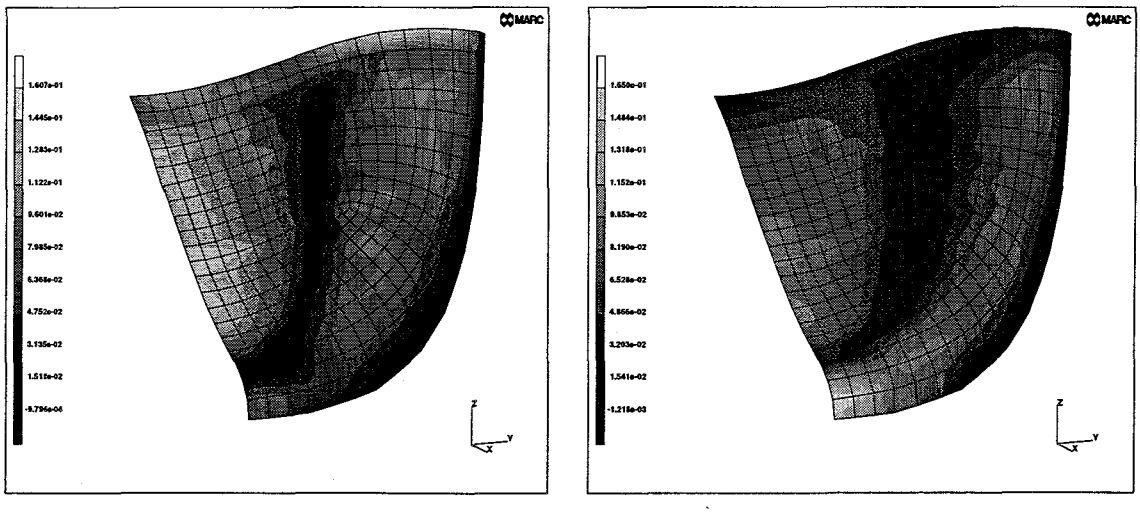

(c) (d)

Figure C.5: *Stress distributions of a unidirectional, circumferential reinforced model with 10 fibers and a fiber modulus of 300 MPa. Maximum longitudinal stresses (a and c) and maximum transversal stresses (b and d) in closed and half closed configurations respectively.*

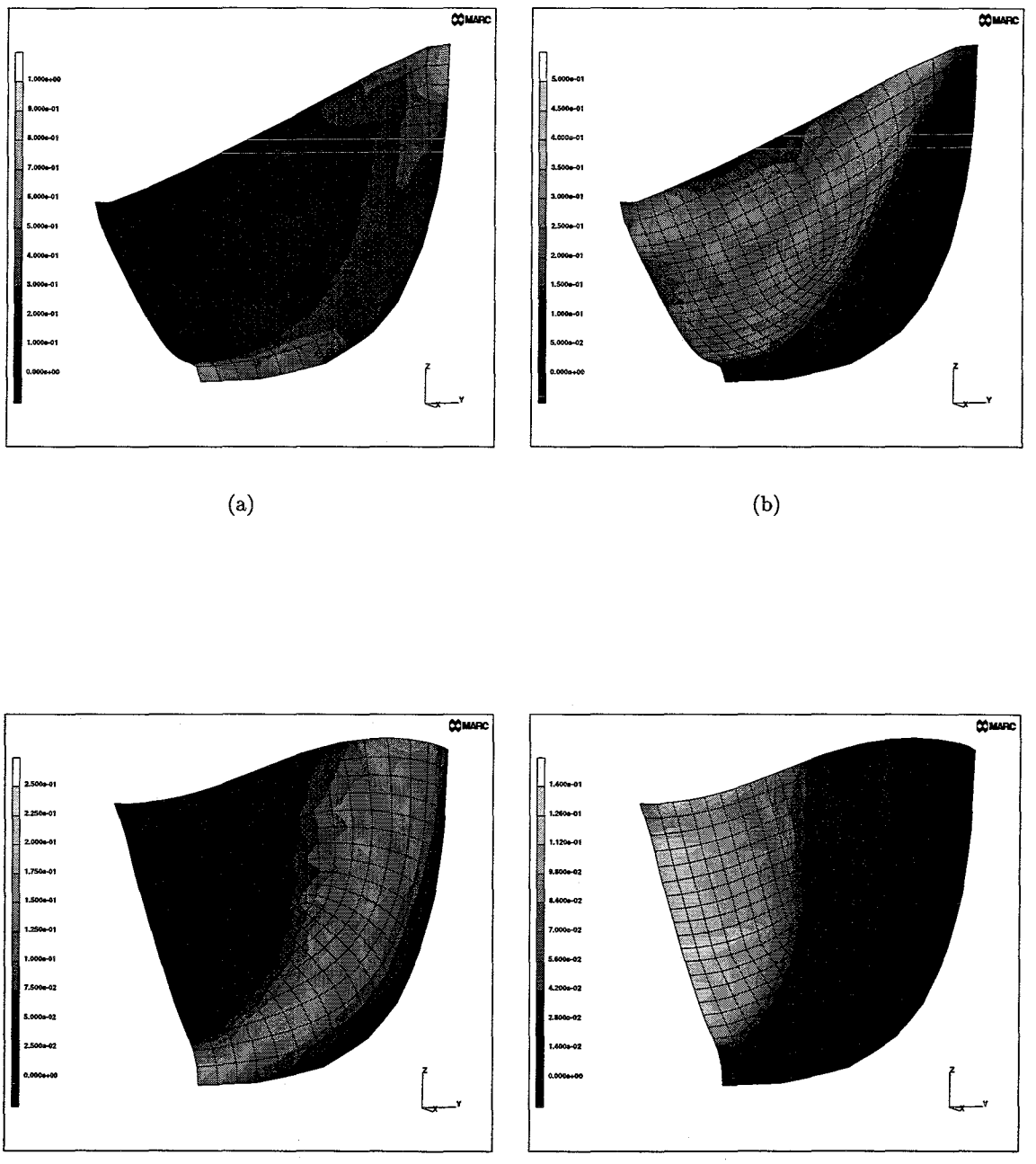

(a) (b)

(c) (d)

Figure C.6: *Stress distributions of a unidirectional, circumferential reinforced model with 10 fibers and a fiber modulus of 3 GPa. Maximum principle stresses in the aortic rubber layer (a and c) and the ventricular rubber layer (b and d) in closed and half closed configurations respectively.*

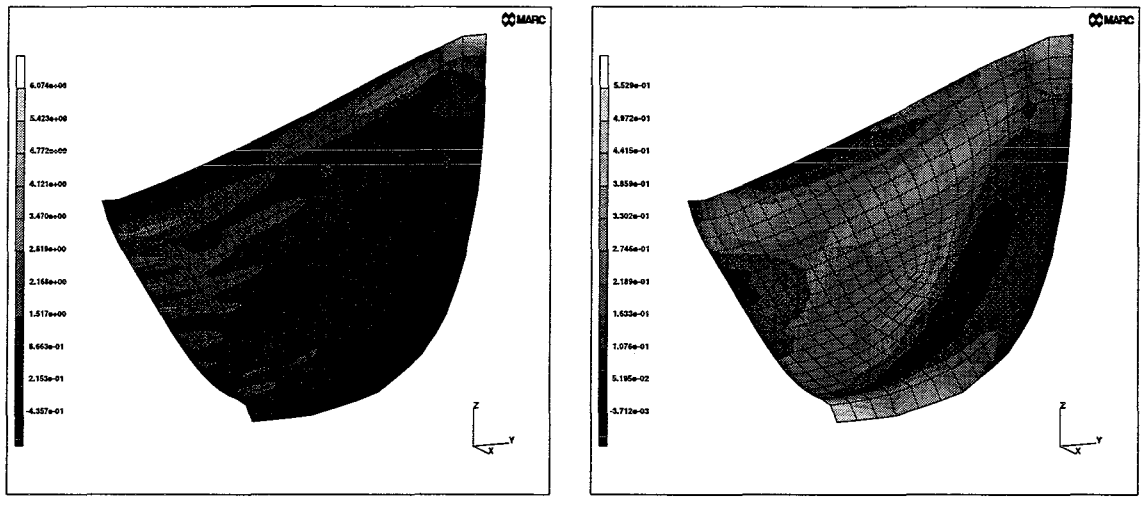

(a) (b)

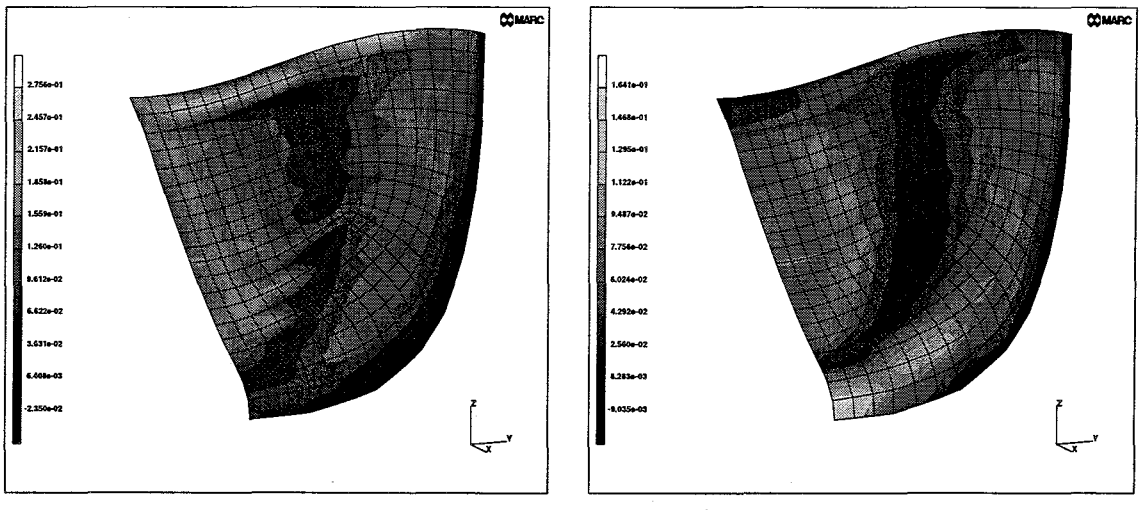

(c) (d)

Figure C.7: *Stress distributions of a unidirectional, circumferential reinforced model with 10 fibers and a fiber modulus of 3 GPa. Maximum longitudinal stresses (a and c) and maximum transversal stresses (b and d) in closed and half closed configurations respectively.*

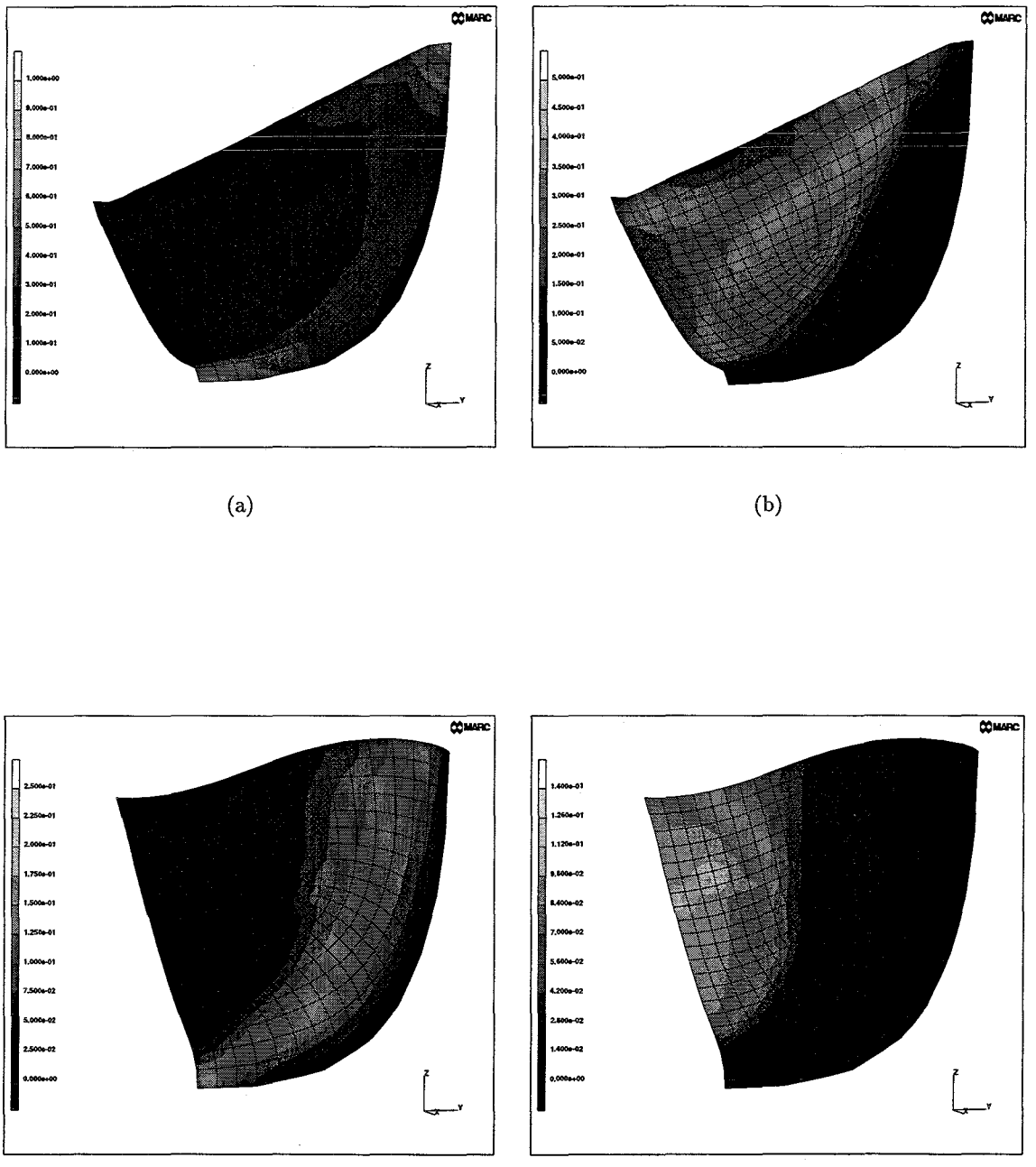

Figure C.8: *Stress distributions of a unidirectional, circumferential reinforced model with 20 fibers and a fiber modulus of 3 GPa. Maximum principle stresses in the aortic rubber layer (a and c) and the ventricular rubber layer (b and d) in closed and half closed configurations respectively.*

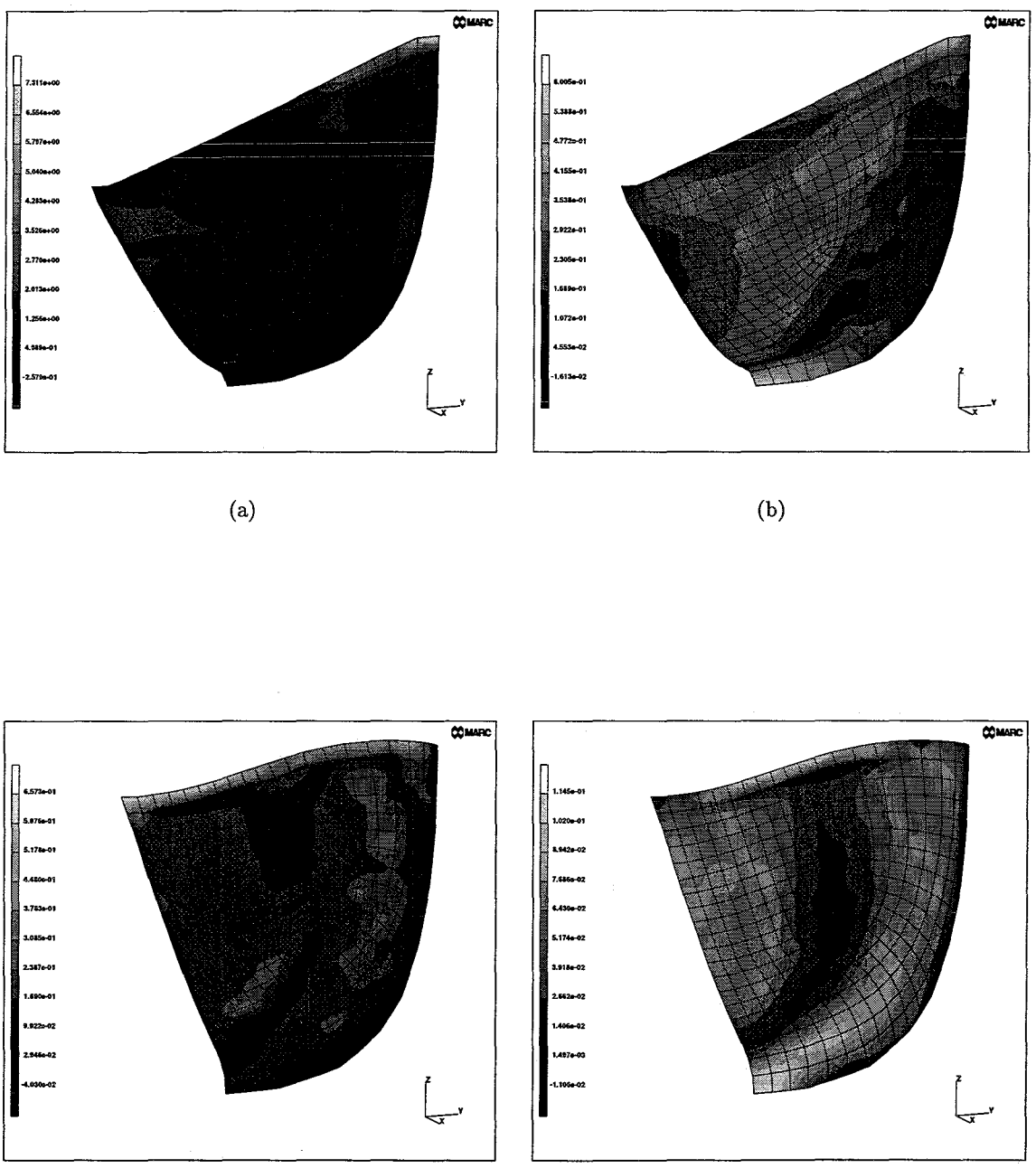

(a) (b)

(c) (d)

Figure C.9: *Stress distributions of a unidirectional, circumferential reinforced model with 20 fibers and a fiber modulus of 3 GPa. Maximum longitudinal stresses (a and c) and maximum transversal stresses (b and d) in closed and half closed configurations respectively.*

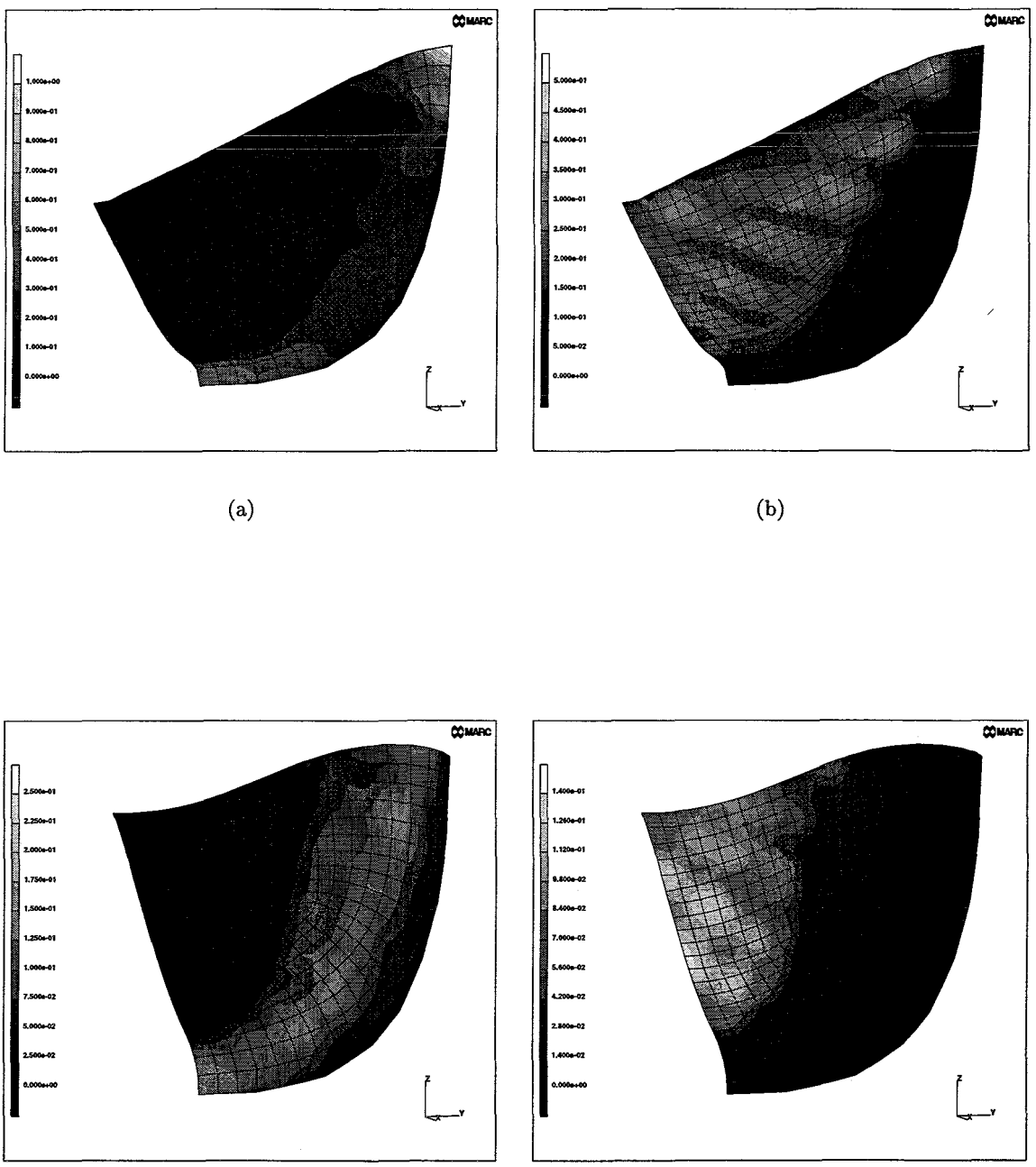

(a) (b)

(c) (d)

Figure C.10: *Stress distributions of a sinusoidal reinforced model with 10 fibers and a fiber modulus of 3 GPa. Maximum principle stresses in the aortic rubber layer (a and c) and the ventricular rubber layer (b and d) in closed and half closed configurations respectively.*

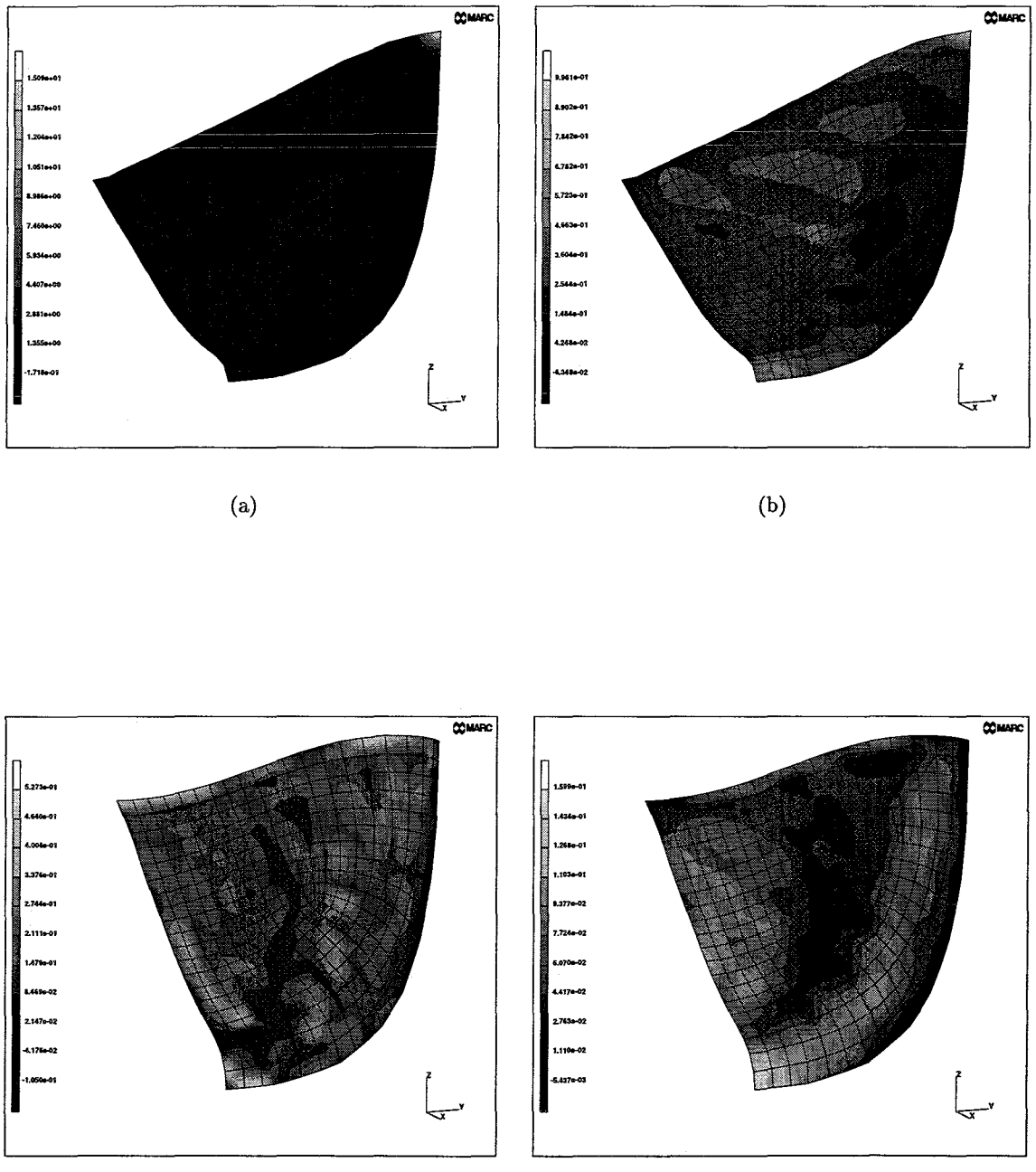

Figure C.11: *Stress distributions of a sinusoidal reinforced model with 10 fibers and a fiber modulus of 3 GPa. Maximum longitudinal stresses (a and c) and maximum transversal stresses (b and d) in closed and half closed configurations respectively.*

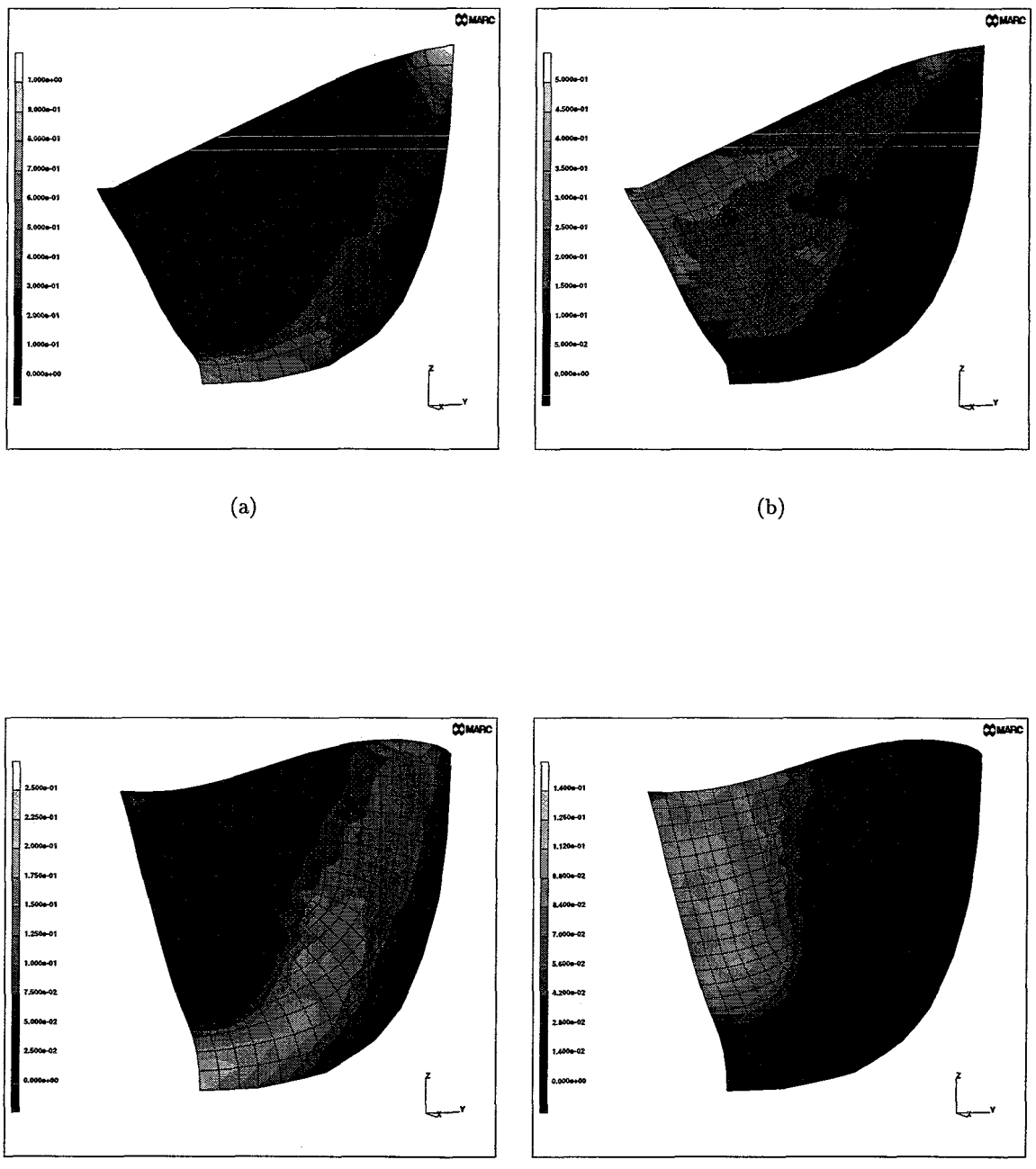

(a) (b)

(c) (d)

Figure C.12: *Stress distributions of a sinusoidal reinforced model with 20 fibers and a fiber modulus of 3 GPa. Maximum principle stresses in the aortic rubber layer (a and c) and the ventricular rubber layer (b and d) in closed and half closed configurations respectively.*

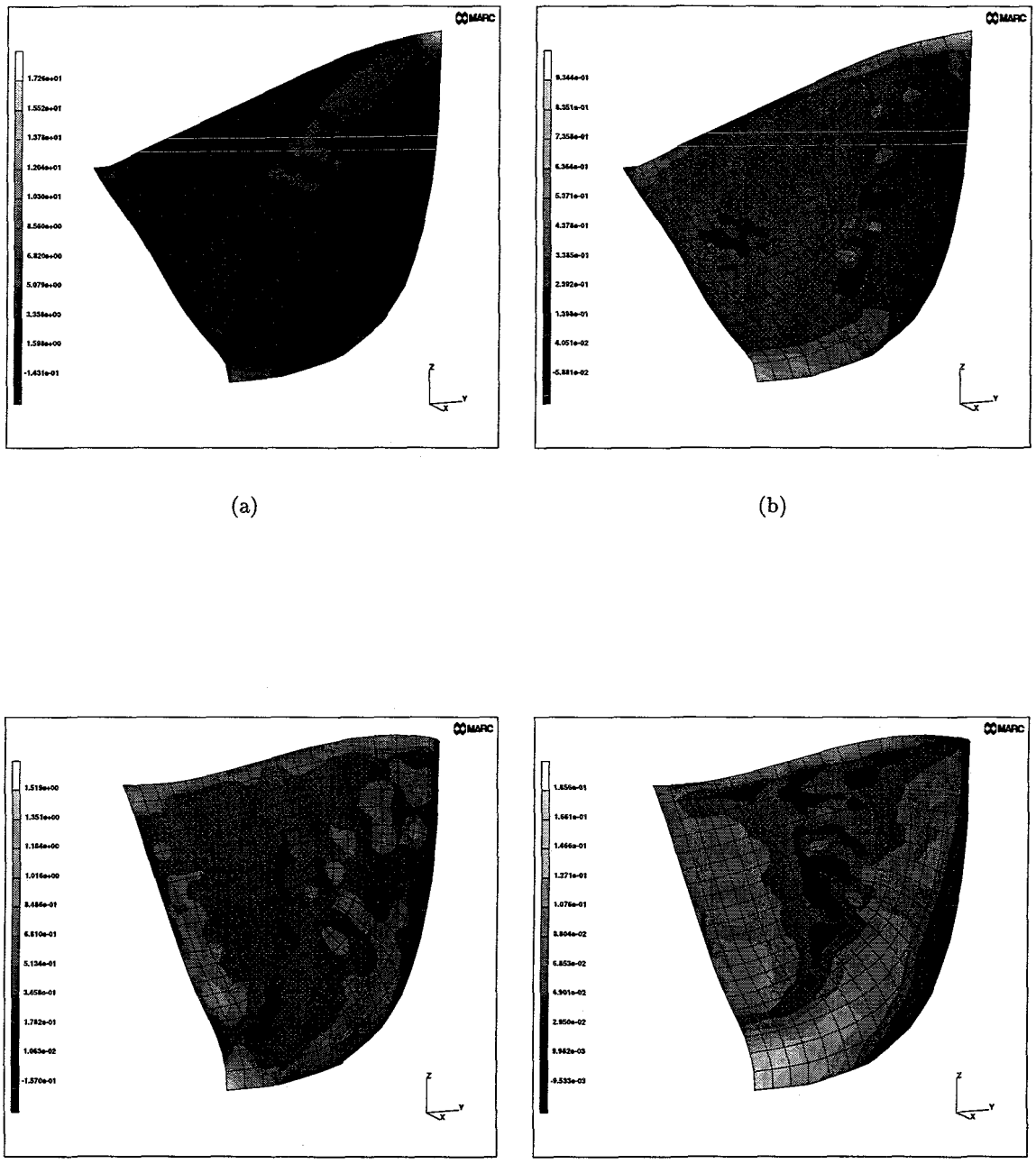

(a) (b)

(c) (d)

Figure C.13: *Stress distributions of a sinusoidal reinforced model with 20 fibers and a fiber modulus of 3 GPa. Maximum longitudinal stresses (a and c) and maximum transversal stresses (b and d) in closed and half closed configurations respectively.*